

# *Swift* follow-up of IceCube triggers, and implications for the Advanced-LIGO era

P. A. Evans,<sup>1★</sup> J. P. Osborne,<sup>1</sup> J. A. Kennea,<sup>2</sup> M. Smith,<sup>3</sup> D. M. Palmer,<sup>4</sup> N. Gehrels,<sup>5</sup> J. M. Gelbord,<sup>6,7</sup> A. Homeier,<sup>8</sup> M. Voge,<sup>8</sup> N. L. Strotjohann,<sup>8,9</sup> D. F. Cowen,<sup>10</sup> S. Böser,<sup>11</sup> M. Kowalski<sup>8,9</sup> and A. Stasik<sup>9</sup>

<sup>1</sup>Department of Physics and Astronomy, University of Leicester, Leicester LE1 7RH, UK

<sup>2</sup>Department of Astronomy and Astrophysics, Pennsylvania State University, 525 Davey Lab, University Park, PA 16802, USA

<sup>3</sup>Jet Propulsion Laboratory, 4800 Oak Grove Drive, Pasadena, CA 91109, USA

<sup>4</sup>Los Alamos National Laboratory, B244, Los Alamos, NM 87545, USA

<sup>5</sup>NASA Goddard Space Flight Center, Greenbelt, MD 20771, USA

<sup>6</sup>Spectral Sciences Inc., 4 Fourth Ave, Burlington, MA 01803, USA

<sup>7</sup>Eureka Scientific Inc., 2452 Delmer St, Suite 100, Oakland, CA 94602, USA

<sup>8</sup>Physikalisches Institut, Universität Bonn, Nußallee 12, D-53115 Bonn, Germany

<sup>9</sup>DESY, D-15735 Zeuthen, Germany

<sup>10</sup>Department of Astronomy and Astrophysics, Pennsylvania State University, University Park, PA 16802, USA

<sup>11</sup>Institute of Physics, University of Mainz, Staudinger Weg 7, D-55099 Mainz, Germany

Accepted 2015 January 17. Received 2015 January 12; in original form 2014 October 24

## ABSTRACT

Between 2011 March and 2014 August *Swift* responded to 20 triggers from the IceCube neutrino observatory, observing the IceCube 50 per cent confidence error circle in X-rays, typically within 5 h of the trigger. No confirmed counterpart has been detected. We describe the *Swift* follow-up strategy and data analysis and present the results of the campaign. We discuss the challenges of distinguishing the X-ray counterpart to a neutrino trigger from serendipitous uncatalogued X-ray sources in the error circle, and consider the implications of our results for future strategies for multimessenger astronomy, with particular reference to the follow-up of gravitational wave triggers from the advanced-era detectors.

**Key words:** gravitational waves – neutrinos – methods: observational – gamma-ray burst: general – X-rays: general.

## 1 INTRODUCTION

For biological reasons, astronomy has been a science carried out using electromagnetic (EM) radiation, and indeed until comparatively recently was limited to that portion of the EM spectrum to which our eyes are sensitive, and the atmosphere transparent. This has changed over the last century and at the present time observatories exist collecting data from the longest wavelengths (e.g. LOFAR<sup>1</sup>) to the shortest (e.g. HESS; Hinton et al. 2004). Today, a growing area of astronomical research does not use EM radiation at all, but probes other messengers, such as neutrinos, gravitational waves or cosmic rays. The detection and identification of astrophysical sources of these messengers is difficult, and an ideal scenario is to combine detections of non-EM messengers with EM signals, to provide a *multimessenger* data set. To date, the only object outside of our Solar system to be detected in this way is the supernova SN1987a (Kunkel et al. 1987), which, in addition to its EM discovery and ob-

servations, was also detected as a neutrino emitter (Alekseev et al. 1987; Bionta et al. 1987; Hirata et al. 1987, 1988). While extrasolar cosmic rays (e.g. Abraham et al. 2010) and PeV neutrinos (Aartsen et al. 2013) have been detected, the origin of these is still unclear and they have not been reliably coupled with a known EM object.

Neutrinos are expected from various sources, such as supernovae (SNe; e.g. Kachelrieß et al. 2005; Abbasi et al. 2014) and gamma-ray bursts (GRBs; e.g. Asano & Mészáros 2014), but targeted searches – retrospectively searching the neutrino data corresponding to the time and location of EM detections of these phenomena – have so far yielded null results from both the IceCube (Abbasi et al. 2011, 2012) and ANTARES (Adrián-Martínez et al. 2013) observatories. Similarly, gravitational waves are expected to arise from a range of phenomena, particularly the merger of two neutron stars in a short GRB. Targeted searches for gravitational waves from short GRBs have also, so far, failed to produce any detections (e.g. Abadie et al. 2010b).

Effort has also been expended to search for EM counterparts to non-EM triggers. Because EM facilities tend to have narrow fields of view, the likelihood of a non-EM trigger being contemporaneously observed by an EM telescope are very low, therefore the EM data

★E-mail: pae9@leicester.ac.uk

<sup>1</sup> <http://www.lofar.org>

have to be collected after the non-EM trigger. The error regions from neutrino or gravitational wave facilities are on the scale of degrees, thus it often requires multiple pointings to collect the necessary EM data. It is also not clear when is the optimal time to search for the counterpart, as the relative time-scales of EM and non-EM radiation depends on the physical source of the emission. For example, for SNe the neutrino signal precedes the EM signal by many days. An optimal follow-up facility would, therefore, have a large (ideally all-sky) field of view, and high level of sensitivity. Due to the high rate of transient events in the Universe, multiwavelength capabilities are also desirable, for example to help distinguish rapidly between GRBs and flare stars.

The *Swift* satellite (Gehrels et al. 2004) arguably provides the best existing facility for the EM follow-up of non-EM triggers, at least in X-rays. Although the X-ray telescope (XRT; Burrows et al. 2005) has only a modest field of view (radius  $\sim 0.2^\circ$ ), the *Swift* spacecraft is capable of rapid slewing, and has the ability to ‘tile’ regions on the sky, so as to cover a large error region in a single spacecraft orbit. The XRT is sensitive to  $5 \times 10^{-13} \text{ erg cm}^{-2} \text{ s}^{-1}$  in 1 ks (0.3–10 keV), and can localize sources to a 90 per cent confidence radius of 3.5 arcsec (improving to 1.4 arcsec for brighter sources; Goad et al. 2007; Evans et al. 2009).

Evans et al. (2012) reported on *Swift* follow-up of two gravitational wave triggers from the LIGO-Virgo (Abbott et al. 2009; Accadia et al. 2012) facilities. No X-ray counterpart to the gravitational triggers could be found, and indeed it transpired that neither of the gravitational wave triggers was in fact real (one was a sub-threshold noise event, the other an artificial signal introduced to the data as a blind test of the detection algorithms). In this work, we report on the search with *Swift*-XRT for X-ray counterparts to 20 neutrino-doublet triggers from the IceCube facility (Achterberg et al. 2006), and discuss the challenges related to identifying the EM counterpart. A neutrino doublet (or multiplet) was defined as two or more neutrinos detected within 100 s of each other, and with an angular separation of at most  $3.5^\circ$ ; more details about this is given in a companion paper (Aartsen et al., in preparation).

The *Swift* follow-up observations began as soon as possible after the neutrino trigger, implicitly assuming that the X-ray emission from the astrophysical neutrino source is temporally coincident with (or only a few hours after) the neutrino emission. We consider two ways of identifying the X-ray counterpart: by its brightness compared to reference catalogues, or by its temporal variability (in particular, whether it shows signs of fading, as may be expected following some form of outburst).

We did not set the threshold at which *Swift* will respond to a neutrino trigger based on theoretical predictions of neutrino flux (which are highly uncertain due to the lack of observational constraint), instead we set it such that IceCube would be expected to produce roughly six spurious (i.e. non-astrophysical) triggers per year, which represents a compromise between sensitivity to astrophysical neutrinos, and the value of *Swift*’s observing time. The companion paper (Aartsen et al., in preparation) will discuss the expected rate of doublet triggers from the background and from astrophysical objects, and consider the lack of neutrino triplets during this experiment.

This paper is organized as follows. In Section 2 we describe the follow-up observing strategy employed by *Swift*, and in Section 3 we overview the data analysis techniques. In Section 4 we consider the sources detected, and attempt to identify if either of these is likely to be the counterpart to the neutrino trigger, which we expect to be a source undergoing some form of outburst. Finally, in Section 5 we consider the implications of our findings for future EM follow-up

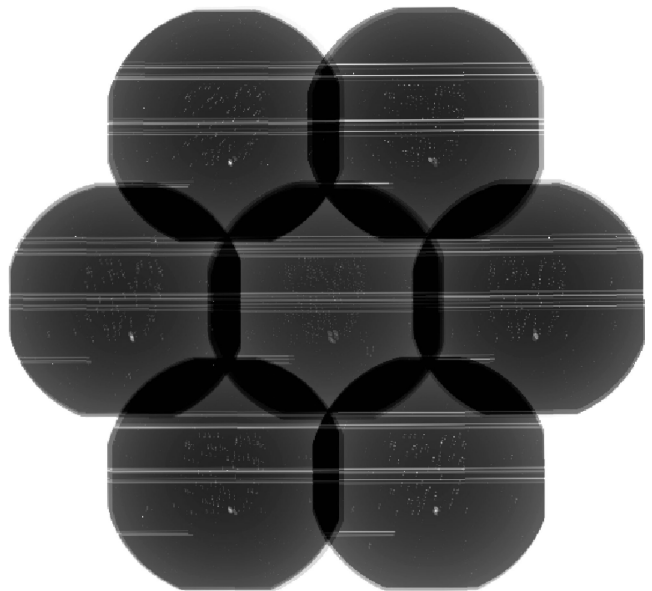


**Figure 1.** An example exposure map of a 7-tile *Swift*-XRT observation of an IceCube trigger. This observation was taken with the on-board tiling, so the exposure in each field has been built up over multiple spacecraft orbits; the pointing is slightly different on each orbit, hence the blurring round the edges of the fields. The black lines and dots are the bad columns and pixels on the CCD.

of non-EM triggers, in particular, the expected gravitational wave triggers from the Advanced-LIGO–Virgo facility.

Throughout the paper we have assumed a cosmology with  $H_0 = 71 \text{ km s}^{-1} \text{ Mpc}^{-1}$ ,  $\Omega_m = 0.27$ ,  $\Omega_{\text{vac}} = 0.73$ . Unless otherwise stated, all quoted errors are at the 90 per cent confidence level, and upper limits at the  $3\sigma$  ( $=99.7$  per cent) confidence level.

## 2 SWIFT’S OBSERVING STRATEGY

Following IceCube triggers, high-priority Target of Opportunity (ToO) requests were submitted to *Swift*. Due to the efficient and flexible operation of *Swift*, observations were able to begin rapidly once the ToO was received: the median time from IceCube trigger to the first *Swift* observation was 1.8 h. The IceCube 50 per cent error radius is typically  $>0.5^\circ$ , whereas the *Swift*-XRT has a field of view of radius of  $0.2^\circ$ , therefore it was necessary to observe the error region in a series of seven overlapping ‘tiles’: an example exposure map is shown in Fig. 1. Initially this tiling had to be performed by manually commanding seven separate observations as *Swift* Automatic Targets;<sup>2</sup> each tile was consequently observed on a separate spacecraft orbit. Under this system, all of the requested exposure in a given tile (typically 1–2 ks) was gathered in a single spacecraft pointing;<sup>3</sup> however, for each successive field the delay between the trigger and the observation increased by  $\sim 96$  min (*Swift*’s orbital period). On 2011 August 10 the software on-board *Swift* was modified to support automatic tiling. In this system, which was used from trigger #3 onwards (Table 1), a single Automatic Target is

<sup>2</sup> That is, the observations were not in the pre-planned science timeline, and overrode targets which were. The times of the observations were set automatically by the on-board software.

<sup>3</sup> XRT can observe a single target for a maximum of 2.7 ks per 96-min spacecraft orbit.

**Table 1.** Details of the 20 IceCube triggers followed up by *Swift* as of 2014 September 03.

Trigger #	Error radius (50 per cent conf)	Trigger time (UT)	Delay <sup>a</sup> (h)	Tiling type
1	0°7	2011-03-26 21:53:41	1.4	Manual
2	0°7	2011-09-27 12:23:29	7.5	Manual
3	0°3	2011-10-24 02:41:11	10.0	Automatic
4	0°7	2011-12-06 01:40:15	1.7	Automatic
5	1°1	2012-01-17 22:01:34	4.8	Automatic
6	0°5	2012-02-08 00:14:29	1.4	Automatic
7	1°8	2012-03-03 16:47:22	1.2	Automatic
8	0°7	2012-08-29 22:49:59	2.5	Automatic
9	0°9	2012-09-17 18:08:03	1.6	Automatic
10	0°8	2012-10-23 04:46:15	5.7	Automatic
11	0°4	2012-12-21 02:17:24	3.7	Automatic
12	1°4	2013-01-15 11:08:46	1.5	Automatic
13	0°7	2013-02-13 18:47:42	1.9	Automatic
14	1°2	2013-03-08 22:15:49	17.0	Automatic
15	0°9	2013-03-27 19:54:12	1.5	Automatic
16	1°3	2013-05-17 15:57:03	0.7	Automatic
17	0°8	2014-01-08 05:29:08	9.0	Automatic
18	0°7	2014-01-17 04:02:10	1.8	Automatic
19	0°3	2014-02-26 19:04:14	3.2	Automatic
20	0°7	2014-08-29 13:54:49	1.1	Automatic

*Note.* <sup>a</sup>The time between the possible neutrino event detected by IceCube and the start of the first observation with the *Swift*-XRT.

uploaded, and *Swift* automatically divides the visibility window of the IceCube trigger location in each spacecraft orbit between the seven tiles. This is repeated on each orbit until the requested exposure time has been gathered for each tile.<sup>4</sup> Under this system, all tiles are usually observed in the first visibility window after the observation is uploaded, however the individual exposures are short, so for a given tile to accumulate its full exposure time takes longer. This strategy is better than the manual-upload approach, since it allows *Swift* to cover the entire search box promptly, increasing the chances of detecting a bright, rapidly fading counterpart (e.g. a GRB afterglow), without significantly reducing the likelihood of finding a slowly fading counterpart. Details of the 20 IceCube triggers are given in Table 1.

### 3 DATA ANALYSIS

The XRT data were automatically analysed at the United Kingdom Swift Science Data Centre at the University of Leicester, using HEASOFT v6.15.1, and the *Swift* CALDB b20090130\_u20111031\_x20131220\_m20140221. The data were first processed using XRTPIPELINE, then a series of source detection and analysis routines were applied. In a previous work, similar to this but relating to gravitational wave triggers (Evans et al. 2012), we noted the need for a source detection system that was optimized for fainter sources. Since then such a system has been developed (Evans et al. 2014), and we used it in this work. It consists of the following steps: filtering the data, creating images and exposure maps,<sup>5</sup> and locating and characterizing sources. The latter step is an

iterative process which uses a combination of sliding-cell detection, background modelling, source PSF (point spread function)-fitting and likelihood tests to detect and localize sources. It also provides a quality flag for each source, which indicates the probability of the source being spurious. 0.3 per cent of sources flagged as *Good* are spurious; this rises to 1 per cent when the *Good* and *Reasonable* sources are considered (*Reasonable* sources on their own have a 7 per cent false positive rate), and 10 per cent when all sources (*Good*, *Reasonable*, and *Poor*) are included (*Poor* sources on their own have a 35 per cent false positive rate, so should be viewed with caution). Full details of this procedure are given in Evans et al. (2014), particularly sections 3.4 and 7 and fig. 3.

The astrometric accuracy of *Swift*-XRT positions, determined using the on-board star trackers, is 3.5 arcsec (90 per cent confidence; Moretti et al. 2007). This can sometimes be improved either by using the UV/optical telescope on *Swift* as a super star-tracker (so-called position enhancement; Goad et al. 2007; Evans et al. 2009), or by aligning detected XRT sources with 2MASS (Skrutskie et al. 2006) objects (Butler 2007; Evans et al. 2014). We tried both of these methods for each position, although in most cases the source was too faint for the former method to work (i.e. the XRT source could not be detected in an exposure corresponding to a single UVOT image), and there were too few XRT/2MASS matches for the latter method to offer a more accurate astrometric solution than the star trackers on *Swift*.

We also built light curves and spectra of each source using the tools developed by Evans et al. (2007, 2009). These provide fully validated products in which all necessary corrections (e.g. for pile up – where multiple photons impact a single pixel in a single CCD frame, and are consequently miscounted as a single event – the presence of dead columns on the XRT CCD, and exposure variation across the image) have been applied. For most objects there were too few counts to produce more than a single light-curve bin, thus the ‘light curve’ is really simply a single brightness measurement. For those objects with sufficient counts, we binned the light curve such that there were at least 15 counts in each bin. The spectra

<sup>4</sup> The minimum time permitted for a continuous exposure is 60 s; if the observing window is not sufficient for all tiles to be observed for at least this duration on a given orbit, then the next orbit will begin with the first unobserved tile.

<sup>5</sup> This step differed in one detail from Evans et al. (2014): in that work images could not exceed  $1000 \times 1000$  pixels in size. We have overcome this limitation so a single image covering all seven tiles and being  $1900 \times 1900$  pixels ( $1^\circ25 \times 1^\circ25$ ) in size is used.

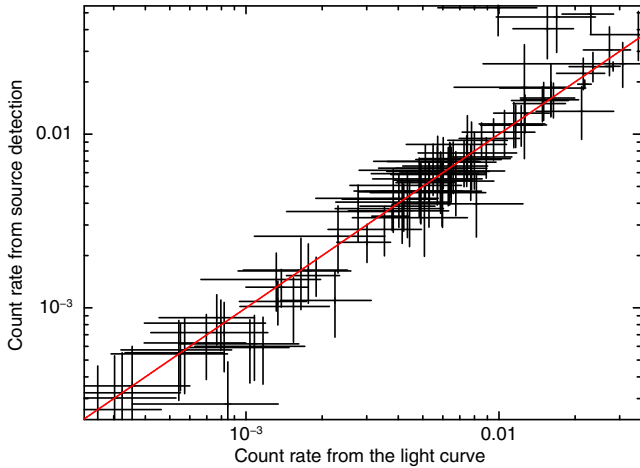


**Figure 2.** The mean source count rates determined from the source detection plotted against the values derived from source light curves, where both are available. The two are in good agreement below  $0.01 \text{ ct s}^{-1}$ , confirming that using the brightness estimates from source detection is a safe approach for the faintest sources for which light curves could not be produced.

were automatically fitted in *XSPEC* (Arnaud 1996) with an absorbed power-law model, using two *TBABS* absorption components (with redshift fixed at 0). One of these was fixed at the Galactic value of  $N_{\text{H}}$  from Willingale et al. (2013), the other was free to vary. The spectral fit was used to determine the energy conversion factor (ECF; conversion from the XRT count rate into an observed 0.3–10 keV flux) for each individual object, and also, via *PIMMS*, a conversion from the measured XRT count rate to the equivalent in the *ROSAT* PSPC (which had an energy coverage of 0.1–2.4 keV; Pfeffermann et al. 1987). The latter conversion allows us to compare the detected sources with the *ROSAT* All-Sky Survey (RASS; Voges et al. 1999): this is the most sensitive all-sky X-ray survey to date and we use it as a reference catalogue (see Section 4.1), along with the *XMM* Slew Survey (XSS; Saxton et al. 2008; Warwick, Saxton & Read 2012) which covers  $\sim 2/3$  of the sky in the 0.2–10 keV band.

For some sources, a light curve or spectrum could not be produced (or the spectrum could not be fitted) as the source was too faint, or too near to the edge of the field of view. Where the light curve could not be produced, the mean count rate was taken from the output of the source detection procedure (which includes corrections for PSF losses, pile up, etc.). These were designed as indicators, and are not fully calibrated. Therefore, to verify their accuracy we compared the mean count rate from the light curve with that from the source detection routine for all sources where both were available. As Fig. 2 shows, the two are in reasonable agreement.

For objects where the automatic spectrum or fit could not be produced, we still require both an ECF and a conversion between the XRT count rate and an equivalent *ROSAT* PSPC rate, to compare the source brightness with the XSS and RASS, respectively. In these cases we used a standard AGN spectral model: an absorbed power law with  $N_{\text{H}} = 3 \times 10^{20} \text{ cm}^{-2}$ , and  $\Gamma = 1.7$ . This yields a 0.3–10 keV ECF of  $4.03 \times 10^{-11} \text{ erg cm}^{-2} \text{ XRT ct}^{-1}$ , and a conversion of 1.497 PSPC counts per XRT count.

In Table 2 we list all of the X-ray objects detected in our follow-up observations, giving their positions, the mean 0.3–10 keV flux, and various parameters which are useful in identifying whether the source is related to the neutrino trigger (described in Section 4.1). The sources for which a spectrum could be constructed and fitted are shown in Table 3 along with details of the spectral fit. A small

number of sources have unconstrained spectral fit parameters, or extreme values which are artefacts of a poor quality spectrum, rather than indicating extreme physical properties. However, since the ECF and PSPC conversion for those sources are compatible with the range seen for the other sources, we do not revert to the standard values given above. One object, source 2 in the field of trigger 1, has a very high ECF which is driven by the fact that the spectrum is very hard, however we have not reverted to the standard AGN spectrum for this, as it is clearly inappropriate. The lack of soft emission from this object means that we do not expect *ROSAT* to have seen it; a fact which would be unclear if we used the standardized spectrum: that is only used for objects where we had no XRT spectral fit at all.

#### 4 IDENTIFYING POTENTIAL COUNTERPARTS TO THE NEUTRINO TRIGGER

Each 7-tile observation with *Swift*-XRT covers  $\sim 0.8 \text{ deg}^2$ , with typical exposures of 1–2 ks per tile. In such exposure times, our detection limit is  $6\text{--}10 \times 10^{-13} \text{ erg cm}^{-2} \text{ s}^{-1}$  (corresponding to 90 per cent completeness; see Evans et al. 2014, fig. 14). This is significantly more sensitive than the RASS, which covers 92 per cent of the sky down to  $0.1 \text{ ct s}^{-1}$  in the PSPC<sup>6</sup> (Voges et al. 1999), which corresponds to  $2.8 \times 10^{-12} \text{ erg cm}^{-2} \text{ s}^{-1}$  in the 0.3–10 keV band covered by XRT (assuming the canonical AGN spectrum described above). For absorbed sources (i.e. with little flux in the *ROSAT* bandpass), the increase in sensitivity of *Swift*-XRT over *ROSAT* is even greater. The XSS provides hard-band coverage, being sensitive to  $\sim 3 \times 10^{-12} \text{ erg cm}^{-2} \text{ s}^{-1}$  in the 2–10 keV band (Warwick et al. 2012), however it only covers  $\sim 2/3$  of the sky. Because of the sensitivity of the XRT compared to these catalogues, and the low spatial coverage of deeper catalogues like 1CSC (Evans et al. 2010),<sup>7</sup> 3XMMi-DR4 (Watson et al., in preparation) and 1SXPS (Evans et al. 2014), we expect to discover uncatalogued X-ray sources that are serendipitously present in the IceCube error region. We therefore need to be able to identify the true X-ray counterpart to the neutrino trigger from among the unrelated objects detected in the field of view. The first step is to remove any sources which are already known X-ray emitters (and are not in outburst at the time of the *Swift* observations). We searched the X-ray Master catalogue<sup>8</sup> for any catalogued X-ray object with a position agreeing with our XRT position at the  $3\sigma$  level (including any systematic errors on the catalogued positions). For all observations after 2012 October<sup>9</sup> we also searched for matches in the 1SXPS catalogue. The sources with catalogue matches are indicated in Table 2, and details of the matches are given in Table 4. In all cases where a match was found, the XRT flux was consistent with (at the  $2\sigma$  level) or occasionally slightly lower than the catalogued flux, therefore these sources were all rejected as possible counterparts.

For the remaining, uncatalogued sources we performed two tests to identify the counterpart: variability tests, and serendipity likelihoods.

<sup>6</sup> For individual fields the RASS limit may be deeper.

<sup>7</sup> No relation.

<sup>8</sup> <http://heasarc.gsfc.nasa.gov/W3Browse/master-catalog/xray.html>;  
<http://ledas-www.star.le.ac.uk/arnie5/arnie5.php?action=basic&catname=xcoll>

<sup>9</sup> That is, the dates covered by the 1SXPS catalogue; the observations of IceCube fields prior to this date are in the 1SXPS catalogue, therefore it cannot be used as a reference in those cases.



**Table 2.** Sources detected in the XRT follow-up of the IceCube triggers.

IceCube field	Src #	Location (J2000)	Err <sup>a</sup> (arcsec)	Flag <sup>b</sup>	Exposure (ks)	<i>C</i> ( <i>B</i> ) <sup>c</sup>	Obs flux <sup>d</sup> ( $\times 10^{-13}$ erg cm <sup>-2</sup> s <sup>-1</sup> ) (0.3–10 keV)	Upper limit <sup>e</sup> ( $\times 10^{-13}$ erg cm <sup>-2</sup> s <sup>-1</sup> ) (0.3–10 keV)	<i>N</i> <sub>seren</sub> <sup>f</sup>	<i>P</i> <sub>const</sub> <sup>g</sup>	Cat <sup>h</sup>
1	1	03 <sup>h</sup> 31 <sup>m</sup> 05 <sup>s</sup> .1 +13° 56′ 00″	3.2★	G	3.5	16 (0.8)	1.81 (±0.48)	12	2.7		
1	2	03 <sup>h</sup> 30 <sup>m</sup> 58 <sup>s</sup> .7 +13° 57′ 06″	5.2	G	3.5	12 (0.8)	1940 (±640)	8	3.7		
1	3 <sup>¶</sup>	03 <sup>h</sup> 31 <sup>m</sup> 01 <sup>s</sup> .8 +14° 15′ 06″	6.1★	G	1.8	8 (0.5)	1.97 (±0.84)	6.9	3.1		
1	4	03 <sup>h</sup> 29 <sup>m</sup> 47 <sup>s</sup> .9 +14° 26′ 37″	4.4★	G	1.5	8 (0.5)	3.8 (±1.6)	33	2.1		
3	1 <sup>¶</sup>	14 <sup>h</sup> 59 <sup>m</sup> 06 <sup>s</sup> .8 +59° 31′ 09″	4.3★	G	1.3	17 (0.5)	5.1 (±1.3)		0.7		Y
3	2	14 <sup>h</sup> 59 <sup>m</sup> 05 <sup>s</sup> .1 +60° 08′ 43″	3.7★	G	1.8	10 (0.6)	3.1 (±1.2)	18	2.3		
3	3 <sup>¶</sup>	15 <sup>h</sup> 01 <sup>m</sup> 06 <sup>s</sup> .8 +59° 59′ 43″	5.7	G	2.1	7 (0.8)	1.79 (±0.76)	7.6	2.6		
4	1 <sup>¶</sup>	22 <sup>h</sup> 15 <sup>m</sup> 02 <sup>s</sup> .5 +57° 02′ 43″	3.5★	G	0.4	16 (0.1)	9.7 (±2.7); 9.3 (±2.1)	15	0.1	0.78	
4	2	22 <sup>h</sup> 15 <sup>m</sup> 03 <sup>s</sup> .2 +57° 02′ 16″	4.0★	G	0.4	10 (0.1)	4.1 (±1.4); 4.03 (±0.85)	4.8	0.1	0.92	
5	1 <sup>¶</sup>	08 <sup>h</sup> 31 <sup>m</sup> 36 <sup>s</sup> .4 +18° 20′ 55″	4.3★	R	0.2	15 (3.5)	4.0 (±1.7)	12	0.3		
5	2 <sup>¶</sup>	08 <sup>h</sup> 31 <sup>m</sup> 10 <sup>s</sup> .8 +18° 33′ 01″	3.2★	G	0.3	14 (3.6)	6.3 (±1.7)	13	0.3		
5	3 <sup>¶</sup>	08 <sup>h</sup> 31 <sup>m</sup> 09 <sup>s</sup> .6 +18° 25′ 37″	3.2★	G	0.8	11 (4.4)	3.8 (+2.1, -1.7) <sup>‡</sup>	10	0.3		
5	4 <sup>¶</sup>	08 <sup>h</sup> 32 <sup>m</sup> 12 <sup>s</sup> .8 +18° 37′ 02″	3.2★	G	0.7	15 (3.8)	6.5 (±2.4)	14	0.3		
5	5 <sup>¶</sup>	08 <sup>h</sup> 31 <sup>m</sup> 38 <sup>s</sup> .0 +18° 37′ 55″	3.2★	R	0.2	7 (2.7)	8.0 (+5.6, -4.3) <sup>‡</sup>	17	0.2		
5	6 <sup>¶</sup>	08 <sup>h</sup> 30 <sup>m</sup> 47 <sup>s</sup> .0 +18° 57′ 09″	5.7	G	0.6	6 (0.2)	4.8 (+2.3, -1.8) <sup>‡</sup>	18	0.4		Y
5	7	08 <sup>h</sup> 30 <sup>m</sup> 28 <sup>s</sup> .9 +18° 46′ 11″	5.8	R	0.4	11 (3.0)	6.6 (+3.1, -2.5) <sup>‡</sup>	5.4	0.2		
5	8 <sup>¶</sup>	08 <sup>h</sup> 30 <sup>m</sup> 28 <sup>s</sup> .8 +18° 46′ 10″	4.0★	R	0.3	9 (4.7)	7.5 (+5.7, -4.6) <sup>‡</sup>	6.3	0.2		
5	9 <sup>¶</sup>	08 <sup>h</sup> 30 <sup>m</sup> 04 <sup>s</sup> .3 +18° 52′ 31″	4.7★	R	0.2	13 (4.3)	19.1 (+8.6, -7.1) <sup>‡</sup>	8.9	0.09		
6	1 <sup>¶</sup>	01 <sup>h</sup> 27 <sup>m</sup> 33 <sup>s</sup> .8 +10° 24′ 09″	5.0★	G	1.4	12 (0.5)	4.2 (±1.4)	13	1.0		
6	2	01 <sup>h</sup> 25 <sup>m</sup> 51 <sup>s</sup> .4 +09° 59′ 24″	5.5	G	1.6	10 (0.5)	2.21 (±0.82)	44	1.7		
6	3	01 <sup>h</sup> 24 <sup>m</sup> 25 <sup>s</sup> .8 +10° 09′ 32″	5.5	G	1.6	9 (0.6)	2.9 (±1.3)	29	3.0		
6	4	01 <sup>h</sup> 24 <sup>m</sup> 45 <sup>s</sup> .2 +10° 07′ 08″	7.0	G	1.6	9 (0.4)	3.2 (±1.2)	32	2.1		
6	5 <sup>¶</sup>	01 <sup>h</sup> 24 <sup>m</sup> 51 <sup>s</sup> .5 +10° 10′ 33″	6.1	G	1.7	7 (0.4)	1.98 (±0.90)	13	3.1		
6	6 <sup>¶</sup>	01 <sup>h</sup> 25 <sup>m</sup> 23 <sup>s</sup> .1 +10° 03′ 23″	8.4	G	1.5	9 (0.5)	2.3 (±1.0)		2.5		Y
6	7	01 <sup>h</sup> 26 <sup>m</sup> 56 <sup>s</sup> .8 +10° 12′ 59″	5.7	G	2.0	7 (0.6)	1.39 (±0.63)	38	3.5		
6	8 <sup>¶</sup>	01 <sup>h</sup> 26 <sup>m</sup> 12 <sup>s</sup> .4 +10° 26′ 27″	10.4	G	1.7	7 (0.6)	2.4 (±1.2)	11	2.3		
6	9 <sup>¶</sup>	01 <sup>h</sup> 25 <sup>m</sup> 52 <sup>s</sup> .7 +10° 22′ 14″	7.7	R	2.8	7 (0.9)	0.93 (±0.50)	9.2	1.4		
6	10	01 <sup>h</sup> 24 <sup>m</sup> 51 <sup>s</sup> .1 +10° 33′ 06″	4.3★	G	1.5	21 (0.5)	4.8 (±2.4); 4.2 (±1.0)	17	0.5	0.71	
6	11	01 <sup>h</sup> 26 <sup>m</sup> 11 <sup>s</sup> .4 +10° 23′ 37″	6.2	G	2.6	9 (0.9)	0.84 (±0.40)	9.0	1.3		
7	1	04 <sup>h</sup> 08 <sup>m</sup> 41 <sup>s</sup> .0 +03° 34′ 37″	1.5★	G	12.9	318 (12.6)	11.3 (±2.1); 5.43 (±0.36)		0.2	5.6 × 10 <sup>-4</sup>	Y
7	2	04 <sup>h</sup> 09 <sup>m</sup> 25 <sup>s</sup> .0 +03° 12′ 37″	6.2	G	2.6	10 (0.8)	1.66 (±0.67)	12	2.8		
7	3 <sup>¶</sup>	04 <sup>h</sup> 09 <sup>m</sup> 42 <sup>s</sup> .9 +03° 19′ 20″	4.8	G	2.1	6 (0.6)	2.04 (±0.98)	15	2.9		Y
7	4	04 <sup>h</sup> 09 <sup>m</sup> 27 <sup>s</sup> .0 +03° 34′ 07″	1.5★	G	18.2	404 (15.7)	22.3 (±5.8); 7.91 (±0.49)	12	0.3	2.6 × 10 <sup>-2</sup>	
7	5	04 <sup>h</sup> 10 <sup>m</sup> 40 <sup>s</sup> .7 +03° 19′ 19″	5.5	G	1.7	9 (0.6)	1.26 (±0.47)	4.2	2.1		
7	6	04 <sup>h</sup> 09 <sup>m</sup> 53 <sup>s</sup> .2 +03° 18′ 48″	7.7	G	2.0	7 (0.8)	1.02 (±0.49)	16	3.0		
7	7	04 <sup>h</sup> 08 <sup>m</sup> 42 <sup>s</sup> .9 +03° 39′ 01″	4.2	G	14.3	46 (4.7)	1.83 (±0.36); 1.57 (±0.26)	35	3.0	0.10	
7	8	04 <sup>h</sup> 09 <sup>m</sup> 27 <sup>s</sup> .8 +03° 30′ 16″	4.3	G	19.0	27 (6.1)	0.94 (±0.41); 0.92 (±0.25)	112	5.1	0.95	
7	9	04 <sup>h</sup> 09 <sup>m</sup> 16 <sup>s</sup> .7 +03° 40′ 19″	5.4	G	17.6	23 (5.7)	1.20 (±0.43); 1.05 (±0.31)	44	5.8	0.46	
7	10	04 <sup>h</sup> 09 <sup>m</sup> 58 <sup>s</sup> .5 +03° 27′ 42″	5.3	G	9.5	26 (3.9)	0.74 (±0.19); 0.70 (±0.17)	7.0	2.4	0.43	
7	11	04 <sup>h</sup> 08 <sup>m</sup> 29 <sup>s</sup> .6 +03° 33′ 03″	5.2	G	4.8	13 (2.0)	1.32 (±0.53)	25	2.2		
7	12	04 <sup>h</sup> 09 <sup>m</sup> 03 <sup>s</sup> .5 +03° 29′ 36″	5.9	G	17.3	16 (6.1)	0.29 (±0.13)	5.6	6.3		
7	13	04 <sup>h</sup> 09 <sup>m</sup> 21 <sup>s</sup> .0 +03° 38′ 04″	5.5	G	18.3	22 (5.8)	0.80 (±0.40)	104	1.2		
7	14	04 <sup>h</sup> 09 <sup>m</sup> 08 <sup>s</sup> .9 +03° 31′ 36″	5.3	G	19.1	17 (6.2)	0.53 (±0.23)	22	8.4		
7	15 <sup>¶</sup>	04 <sup>h</sup> 09 <sup>m</sup> 36 <sup>s</sup> .7 +03° 31′ 59″	5.2	G	17.8	14 (5.6)	0.44 (±0.22)	9.9	7.5		
7	16 <sup>¶</sup>	04 <sup>h</sup> 09 <sup>m</sup> 54 <sup>s</sup> .8 +03° 33′ 47″	7.0	P	16.6	16 (5.7)	0.30 (±0.16); 0.28 (±0.12)	6.2	13.6	0.69	
7	17	04 <sup>h</sup> 08 <sup>m</sup> 43 <sup>s</sup> .0 +03° 33′ 50″	5.9	R	14.8	23 (5.1)	1.59 (±0.42); 1.32 (±0.31)	175	3.5	0.12	
7	18	04 <sup>h</sup> 09 <sup>m</sup> 12 <sup>s</sup> .3 +03° 42′ 34″	5.0	G	17.2	19 (5.8)	0.33 (±0.18); 0.33 (±0.13)	14	6.8	0.98	
7	19	04 <sup>h</sup> 09 <sup>m</sup> 40 <sup>s</sup> .6 +03° 46′ 28″	7.0	P	7.3	11 (2.3)	0.42 (±0.21)	9.6	5.6		
7	20	04 <sup>h</sup> 09 <sup>m</sup> 24 <sup>s</sup> .9 +03° 46′ 25″	10.8	G	9.8	11 (3.2)	0.75 (±0.45); 0.61 (±0.24)	12	4.7	0.58	
7	21 <sup>¶</sup>	04 <sup>h</sup> 09 <sup>m</sup> 59 <sup>s</sup> .2 +03° 44′ 11″	9.7	R	6.2	12 (2.1)	0.71 (±0.34)	11	5.6		
7	22	04 <sup>h</sup> 09 <sup>m</sup> 16 <sup>s</sup> .7 +03° 29′ 38″	5.3	G	18.4	15 (6.1)	0.54 (+0.26, -0.21) <sup>‡</sup>	39	17.5		
7	23	04 <sup>h</sup> 10 <sup>m</sup> 10 <sup>s</sup> .3 +03° 33′ 34″	6.8	R	8.0	10 (3.0)	0.65 (±0.39); 0.39 (±0.15)	6.5	2.8	0.12	
7	24 <sup>¶</sup>	04 <sup>h</sup> 08 <sup>m</sup> 28 <sup>s</sup> .1 +03° 37′ 55″	8.8	R	4.1	7 (1.2)	0.66 (+0.35, -0.27) <sup>‡</sup>	13	4.0		
7	25 <sup>¶</sup>	04 <sup>h</sup> 09 <sup>m</sup> 43 <sup>s</sup> .6 +03° 28′ 35″	5.9	P	17.7	10 (6.2)	0.122 (+0.091, -0.074) <sup>‡</sup>	7.9	16.6		
7	26 <sup>¶</sup>	04 <sup>h</sup> 10 <sup>m</sup> 00 <sup>s</sup> .1 +03° 36′ 23″	6.2	P	15.1	6 (1.4)	0.23 (+0.12, -0.10) <sup>‡</sup>	7.8	13.9		
7	27 <sup>¶</sup>	04 <sup>h</sup> 09 <sup>m</sup> 30 <sup>s</sup> .9 +03° 29′ 53″	5.4	R	19.0	12 (6.1)	0.34 (±0.20)	8.7	9.9		
7	28 <sup>¶</sup>	04 <sup>h</sup> 09 <sup>m</sup> 21 <sup>s</sup> .7 +03° 27′ 40″	6.5	P	17.0	12 (5.7)	0.143 (+0.099, -0.080) <sup>‡</sup>	12	22.0		
7	29 <sup>¶</sup>	04 <sup>h</sup> 09 <sup>m</sup> 16 <sup>s</sup> .1 +03° 39′ 06″	5.1	R	18.1	11 (5.7)	0.131 (+0.091, -0.074) <sup>‡</sup>	7.1	20.1		
7	30 <sup>¶</sup>	04 <sup>h</sup> 08 <sup>m</sup> 54 <sup>s</sup> .9 +03° 27′ 31″	8.1	P	15.1	6 (1.1)	0.139 (+0.078, -0.064) <sup>‡</sup>	10	18.5		
7	31 <sup>¶</sup>	04 <sup>h</sup> 10 <sup>m</sup> 01 <sup>s</sup> .5 +03° 30′ 24″	7.1	P	13.0	13 (4.7)	0.52 (±0.39); 0.33 (±0.16)	10	12.5	0.31	
7	32 <sup>¶</sup>	04 <sup>h</sup> 09 <sup>m</sup> 06 <sup>s</sup> .0 +03° 37′ 12″	5.3	P	19.8	6 (2.1)	0.105 (+0.082, -0.067) <sup>‡</sup>	8.9	2.86		
9	1	04 <sup>h</sup> 03 <sup>m</sup> 51 <sup>s</sup> .5 +05° 10′ 47″	4.7†	G	1.8	10 (0.2)	3.19 (±0.86)	16	1.1		
9	2 <sup>¶</sup>	04 <sup>h</sup> 03 <sup>m</sup> 06 <sup>s</sup> .3 +04° 44′ 13″	7.1	G	0.5	8 (0.1)	8.4 (±3.4)		0.3		Y
9	3	04 <sup>h</sup> 03 <sup>m</sup> 43 <sup>s</sup> .1 +05° 16′ 28″	5.9†	G	1.6	8 (0.7)	0.95 (±0.44)	10	3.2		
9	4 <sup>¶</sup>	04 <sup>h</sup> 04 <sup>m</sup> 28 <sup>s</sup> .5 +05° 18′ 44″	4.3†	G	1.5	15 (0.5)	4.9 (±1.3)		0.8		Y
9	5 <sup>¶</sup>	04 <sup>h</sup> 03 <sup>m</sup> 09 <sup>s</sup> .6 +05° 27′ 27″	5.9†	G	1.5	6 (0.3)	1.70 (±0.85)	10	3.4		
10	1 <sup>¶</sup>	22 <sup>h</sup> 39 <sup>m</sup> 49 <sup>s</sup> .1 +06° 06′ 00″	5.5	G	0.3	10 (0.2)	14.3 (±5.1)		0.1		Y
10	2 <sup>¶</sup>	22 <sup>h</sup> 40 <sup>m</sup> 32 <sup>s</sup> .6 +06° 39′ 59″	5.0	G	1.3	13 (0.3)	4.6 (+1.5, -1.3) <sup>‡</sup>	18	0.8		

Table 2 – continued

IceCube field	Src #	Location (J2000)	Err <sup>a</sup> (arcsec)	Flag <sup>b</sup>	Exposure (ks)	C (B) <sup>c</sup>	Obs flux <sup>d</sup> ( $\times 10^{-13}$ erg cm <sup>-2</sup> s <sup>-1</sup> ) (0.3–10 keV)	Upper limit <sup>e</sup> ( $\times 10^{-13}$ erg cm <sup>-2</sup> s <sup>-1</sup> ) (0.3–10 keV)	N <sub>seren</sub> <sup>f</sup>	P <sub>const</sub> <sup>g</sup>	Cat? <sup>h</sup>
10	3 <sup>¶</sup>	22 <sup>h</sup> 38 <sup>m</sup> 49 <sup>s</sup> .7 +06° 31′ 10″	6.5	G	0.9	6 (0.4)	3.1 (+1.6, −1.2) <sup>‡</sup>	13	1.0		
11	1 <sup>¶</sup>	14 <sup>h</sup> 14 <sup>m</sup> 58 <sup>s</sup> .2 +07° 41′ 49″	5.8	G	1.7	10 (0.7)	2.66 (±0.98)	7.0	1.1		
11	2 <sup>¶</sup>	14 <sup>h</sup> 15 <sup>m</sup> 47 <sup>s</sup> .1 +08° 08′ 10″	3.3 <sup>*</sup>	G	1.3	28 (0.8)	9.5 (±1.8)		0.1		Y
12	1 <sup>¶</sup>	23 <sup>h</sup> 47 <sup>m</sup> 47 <sup>s</sup> .9 +20° 32′ 02″	7.6	G	0.4	6 (0.1)	7.1 (+3.4, −2.6) <sup>‡</sup>	5.2	0.4		
13	1	10 <sup>h</sup> 57 <sup>m</sup> 46 <sup>s</sup> .9 +36° 15′ 39″	6.1	G	0.8	9 (0.3)	8.3 (±2.8)	16	0.3		Y
13	2 <sup>¶</sup>	10 <sup>h</sup> 58 <sup>m</sup> 17 <sup>s</sup> .1 +35° 30′ 30″	6.8	G	1.7	9 (0.6)	2.40 (+0.96, −0.77) <sup>‡</sup>	19	2.3		
13	3 <sup>¶</sup>	10 <sup>h</sup> 57 <sup>m</sup> 02 <sup>s</sup> .8 +35° 35′ 22″	8.6	G	2.5	10 (1.0)	1.72 (+0.68, −0.55) <sup>‡</sup>	10	3.4		Y
13	4 <sup>¶</sup>	10 <sup>h</sup> 56 <sup>m</sup> 31 <sup>s</sup> .9 +35° 41′ 52″	5.8	G	1.3	7 (0.4)	2.54 (+1.16, −0.90) <sup>‡</sup>	10	2.1		Y
13	5 <sup>¶</sup>	10 <sup>h</sup> 58 <sup>m</sup> 33 <sup>s</sup> .3 +36° 12′ 32″	8.9	G	1.4	7 (0.8)	2.12 (+1.03, −0.80) <sup>‡</sup>	10	2.9		Y
14	1	09 <sup>h</sup> 38 <sup>m</sup> 14 <sup>s</sup> .9 +02° 00′ 23″	4.4	G	1.5	20 (0.5)	7.3 (±3.6); 5.0 (±1.3)		0.5	0.26	Y
14	2 <sup>¶</sup>	09 <sup>h</sup> 37 <sup>m</sup> 08 <sup>s</sup> .6 +01° 25′ 50″	6.4	G	1.5	7 (0.4)	2.06 (±0.94)		2.9		Y
14	3 <sup>¶</sup>	09 <sup>h</sup> 37 <sup>m</sup> 28 <sup>s</sup> .4 +01° 35′ 12″	6.1	G	2.1	8 (0.9)	3.3 (±1.7)	7.9	1.4		
14	4	09 <sup>h</sup> 39 <sup>m</sup> 09 <sup>s</sup> .2 +01° 44′ 38″	5.1	G	1.4	14 (0.6)	4.4 (±1.2)	9.6	0.8		Y
14	5 <sup>¶</sup>	09 <sup>h</sup> 37 <sup>m</sup> 46 <sup>s</sup> .5 +02° 08′ 04″	5.9	G	1.6	7 (0.4)	2.03 (+0.93, −0.72) <sup>‡</sup>	12	2.9		
15	1	18 <sup>h</sup> 57 <sup>m</sup> 53 <sup>s</sup> .8 +02° 40′ 08″	5.2	G	2.4	20 (1.3)	13.0 (±7.3); 9.7 (±2.6)		1.3	0.47	Y
15	2 <sup>¶</sup>	18 <sup>h</sup> 57 <sup>m</sup> 41 <sup>s</sup> .1 +02° 42′ 07″	4.2 <sup>†</sup>	G	2.1	13 (1.2)	2.93 (±0.99)		1.7		Y
15	3 <sup>¶</sup>	18 <sup>h</sup> 58 <sup>m</sup> 09 <sup>s</sup> .8 +02° 21′ 27″	4.8	G	0.5	12 (0.2)	12.4 (±8.9)		0.2		Y
15	4 <sup>¶</sup>	18 <sup>h</sup> 59 <sup>m</sup> 35 <sup>s</sup> .8 +02° 42′ 01″	7.3	G	1.6	7 (0.8)	2.13 (±0.94)	7.2	2.7		
16	1 <sup>¶</sup>	12 <sup>h</sup> 47 <sup>m</sup> 06 <sup>s</sup> .6 +15° 12′ 37″	4.2 <sup>†</sup>	G	1.4	11 (0.7)	3.6 (+1.3, −1.1) <sup>‡</sup>	12	1.1		Y
16	2 <sup>¶</sup>	12 <sup>h</sup> 45 <sup>m</sup> 46 <sup>s</sup> .9 +14° 36′ 27″	5.7 <sup>†</sup>	G	0.7	9 (0.4)	5.9 (+2.3, −1.9) <sup>‡</sup>	11	0.6		
16	3 <sup>¶</sup>	12 <sup>h</sup> 45 <sup>m</sup> 37 <sup>s</sup> .6 +14° 48′ 57″	4.8 <sup>†</sup>	G	0.8	10 (0.4)	5.6 (+2.1, −1.7) <sup>‡</sup>	15	0.6		Y
16	4 <sup>¶</sup>	12 <sup>h</sup> 45 <sup>m</sup> 35 <sup>s</sup> .6 +14° 40′ 11″	5.3 <sup>†</sup>	G	0.8	10 (0.4)	6.0 (+2.2, −1.8) <sup>‡</sup>	13	0.6		Y
16	5 <sup>¶</sup>	12 <sup>h</sup> 45 <sup>m</sup> 37 <sup>s</sup> .9 +14° 56′ 36″	5.1 <sup>†</sup>	G	1.5	10 (0.6)	2.97 (+1.11, −0.90) <sup>‡</sup>	11	1.3		Y
18	1	19 <sup>h</sup> 55 <sup>m</sup> 03 <sup>s</sup> .6 +45° 37′ 04″	5.3	G	1.6	9 (0.6)	3.4 (±1.2)	6.4	1.6		
18	2 <sup>¶</sup>	19 <sup>h</sup> 58 <sup>m</sup> 25 <sup>s</sup> .8 +45° 23′ 29″	11.0	G	1.5	8 (0.5)	2.4 (±1.1)		2.4		Y
18	3 <sup>¶</sup>	19 <sup>h</sup> 58 <sup>m</sup> 01 <sup>s</sup> .7 +45° 18′ 06″	5.6	G	1.6	7 (0.7)	2.4 (±1.0)		2.4		Y
18	4 <sup>¶</sup>	19 <sup>h</sup> 54 <sup>m</sup> 45 <sup>s</sup> .1 +45° 43′ 43″	5.1	G	1.4	7 (0.6)	2.7 (±1.1)	8.8	1.9		
18	5 <sup>¶</sup>	19 <sup>h</sup> 59 <sup>m</sup> 28 <sup>s</sup> .8 +45° 17′ 43″	7.8	G	1.5	8 (0.6)	2.5 (±1.1)	8.4	2.5		
18	6 <sup>¶</sup>	19 <sup>h</sup> 58 <sup>m</sup> 07 <sup>s</sup> .6 +45° 35′ 49″	4.9	G	1.6	10 (0.5)	2.43 (±0.97)	7.9	2.3		
18	7 <sup>¶</sup>	19 <sup>h</sup> 58 <sup>m</sup> 39 <sup>s</sup> .9 +46° 01′ 38″	7.0	G	1.8	7 (0.6)	1.54 (±0.78)	6.6	3.5		
18	8	19 <sup>h</sup> 58 <sup>m</sup> 41 <sup>s</sup> .5 +45° 34′ 11″	9.7	P	3.0	5 (0.2)	0.74 (±0.41)	9.6	0.04		
19	1	10 <sup>h</sup> 21 <sup>m</sup> 00 <sup>s</sup> .7 +16° 25′ 54″	4.7	G	1.3	24 (0.6)	5.5 (±1.3); 5.1 (±1.1)		0.3	0.33	Y
19	2	10 <sup>h</sup> 21 <sup>m</sup> 28 <sup>s</sup> .6 +17° 12′ 44″	4.7	G	2.4	16 (1.0)	1.97 (±0.52)	12	1.3		Y
19	3	10 <sup>h</sup> 22 <sup>m</sup> 49 <sup>s</sup> .1 +16° 53′ 45″	4.9	G	1.4	17 (0.5)	7.4 (±1.9)	26	0.6		
19	4	10 <sup>h</sup> 21 <sup>m</sup> 51 <sup>s</sup> .5 +16° 34′ 32″	6.1	G	1.3	7 (0.5)	4.6 (±2.0)	44	2.1		
19	5 <sup>¶</sup>	10 <sup>h</sup> 21 <sup>m</sup> 18 <sup>s</sup> .2 +17° 12′ 29″	5.2	G	1.3	8 (0.4)	3.2 (±1.2)	24	1.5		Y
19	6 <sup>¶</sup>	10 <sup>h</sup> 19 <sup>m</sup> 35 <sup>s</sup> .0 +16° 52′ 54″	7.3	G	1.5	9 (0.6)	2.71 (+1.09, −0.87) <sup>‡</sup>	16	1.9		
19	7 <sup>¶</sup>	10 <sup>h</sup> 21 <sup>m</sup> 48 <sup>s</sup> .5 +17° 03′ 57″	8.7	R	2.4	7 (0.9)	1.19 (+0.59, −0.46) <sup>‡</sup>	8.3	1.1		
20	1	17 <sup>h</sup> 49 <sup>m</sup> 35 <sup>s</sup> .9 +04° 22′ 29″	3.2 <sup>*</sup>	G	1.6	21 (1.2)	3.3 (±1.4); 3.15 (±0.74)	10	0.6	0.88	Y
20	2	17 <sup>h</sup> 50 <sup>m</sup> 16 <sup>s</sup> .7 +04° 22′ 07″	5.3	G	1.6	9 (1.4)	2.85 (±0.98)		1.3		Y
20	3 <sup>¶</sup>	17 <sup>h</sup> 47 <sup>m</sup> 47 <sup>s</sup> .0 +04° 53′ 37″	5.7	G	0.9	7 (0.5)	3.0 (±1.3)	14	1.5		

Notes. <sup>a</sup>Radius, 90 per cent confidence.

<sup>b</sup>G=Good, R=Reasonable, P=Poor; see text for details.

<sup>c</sup>Number of counts found in the region used to detect the source, with the number expected from the background in parentheses.

<sup>d</sup>This is the observed (i.e. absorbed) flux. For objects with more than one light-curve bin, the peak flux and mean flux are given.

<sup>e</sup>3 $\sigma$  upper limit, from the RASS unless otherwise indicated. If no value is given, this is because the source is a known X-ray emitter, so an upper limit is unnecessary.

<sup>f</sup>The number of sources at least as bright as this one, expected in the XRT field of view. See Section 4.2 for details.

<sup>g</sup>The probability that the source is constant, from a  $\chi^2$  test. Only available if the light curve contained at least two bins.

<sup>h</sup>Whether a catalogued source was found which matched this object; details are given in Table 4.

\*Position enhanced by UVOT astrometry.

†Position derived from XRT-2MASS astrometry.

¶No XRT spectral fit was available, generic AGN spectrum assumed.

‡No XRT light curve was available: the brightness was estimated by the source detection routine.

§This was a very hard source to which *ROSAT* was insensitive, therefore an RASS limit is uninformative.

#### 4.1 Variability

The simplest test of whether an uncatalogued X-ray source is likely to be related to the neutrino trigger is to ask whether the source brightness is such that it should have been seen previously, i.e. the measured brightness is significantly above the sensitivity limit of any instruments which have previously observed the source location without discovering the source. If this is the case then the source is

in a bright state compared to previous observations, and is thus a good candidate to be the counterpart.

For each uncatalogued source, we therefore derived a 3 $\sigma$  upper limit on the *ROSAT* PSPC count rate using images, background maps, and exposure maps obtained from <ftp://ftp.xray.mpe.mpg.de/ftp/rosat/archive>, and the Bayesian method of Kraft, Burrows & Nousek (1991). Where available, we also obtained 3 $\sigma$  upper limits on the 0.2–12 keV flux from the XSS

**Table 3.** Details of the X-ray sources with spectra.

IceCube field	Source #	$N_{\text{H,Gal}}^a$ ( $\times 10^{20} \text{ cm}^{-2}$ )	$N_{\text{H,intr}}^b$ ( $\times 10^{20} \text{ cm}^{-2}$ )	Photon index	ECF <sup>c</sup> ( $\times 10^{-11} \text{ erg cm}^{-2} \text{ ct}^{-1}$ )	PSPC <sup>d</sup>
1	1	27.77	<44.1	1.95 (+1.32, −0.70)	3.4	1.11
1	2	27.70	<260	<0.2	4600	0.01
1	4	26.44	<87.9	1.11 (+1.40, −0.95)	6.1	0.69
3	2	0.93	<34.0	1.06 (+1.15, −0.80)	5.7	1.18
4	2	92.67	<37.6	11.03 (+2.81, −0.72)	1.5	1.74
5	7	3.35	<411	2.4 (+2.2, −1.3)	2.4	1.43
6	2	7.45	821 (+1130, −790)	7.4 (+26.5, −6.8)	3.0	0.31
6	3	6.64	<899.4	1.1 (+1.9, −1.0)	5.7	0.85
6	4	6.82	<48.1	1.27 (+1.01, −0.75)	4.9	0.98
6	7	8.23	<1004	3.8 (+3.2, −4.4)	3.4	0.28
6	10	6.54	<46	2.38 (+2.05, −0.90)	2.6	1.45
6	11	7.54	<69.4	1.72 (+2.26, −0.85)	3.0	1.22
7	1	21.64	<6.2	3.39 (+0.36, −0.19)	1.9	1.65
7	2	21.43	<56.0	1.32 (+1.53, −0.80)	4.1	0.84
7	4	21.20	<12.5	1.96 (+0.26, −0.20)	3.6	1.15
7	5	20.62	<116	5.2 (+12.9, −2.2)	2.0	1.81
7	6	21.13	<502	3.0 (+7.0, −2.7)	2.3	1.01
7	7	21.46	<85	1.64 (+1.04, −0.57)	4.1	0.86
7	8	21.31	240 (+546, −218)	2.05 (+0.93, −0.85)	6.7	0.24
7	9	21.27	<74	0.67 (+1.14, −0.70)	7.8	0.52
7	10	20.99	<39.9	2.30 (+1.30, −0.55)	2.3	1.34
7	11	21.72	<44.7	1.43 (+1.25, −0.84)	3.7	0.90
7	12	21.48	<42.1	2.6 (+2.1, −1.0)	2.5	1.44
7	13	21.24	<355	1.1 (+2.0, −1.1)	10.0	0.35
7	14	21.43	<344	2.2 (+2.9, −1.0)	5.1	0.48
7	17	21.62	<305	1.24 (+2.82, −0.61)	7.0	0.55
7	18	21.30	<99.5	1.37 (+2.08, −0.92)	4.3	0.87
7	19	21.24	<95	1.8 (+1.7, −1.5)	3.2	1.08
7	20	21.26	<61.0	1.50 (+1.51, −0.79)	4.0	0.94
7	22	21.38	<89.1	1.2 (+1.9, −1.1)	9.8	0.81
7	23	20.97	541 (1950, −225.0)	10.1 (+82.8, −7.0)	1.7	1.04
7	30	21.56	39050 (+10 000, −8000)	>50	2.6	1.50
9	1	19.15	<200	2.6 (+3.4, −1.9)	3.4	1.08
9	3	19.01	<497	5.4 (+4.5, −4.8)	2.0	1.10
13	1	2.75	<28.8	1.6 (+1.3, −1.0)	3.9	1.49
14	1	3.44	<21.4	2.37 (+1.44, −0.54)	3.1	2.10
14	4	3.89	<34.0	1.91 (+2.13, −0.64)	3.7	1.56
15	1	144.00	<1312.4	1.4 (+3.3, −2.2)	11.4	0.06
18	1	26.20	<54.7	1.63 (+1.27, −0.88)	4.3	0.96
18	5	32.40	37200 (6300, −13 200)	<sup>e</sup>	4.4	1.50
18	8	30.30	<476.9	1.3 (+3.4, −2.0)	4.1	0.76
19	1	3.11	<18.6	2.40 (+1.49, −0.39)	2.4	2.27
19	2	2.90	<93.5	2.70 (+4.96, −0.88)	2.2	1.68
19	3	2.90	<31.8	1.33 (+1.05, −0.56)	4.9	1.18
19	4	3.02	<274.9	0.59 (+1.42, −0.92)	7.2	0.65
20	1	16.55	<31.9	2.84 (+1.47, −0.78)	2.1	1.55
20	2	16.30	<79.9	1.36 (+1.15, −0.96)	4.9	0.91

Notes. <sup>a</sup>The Galactic absorption value, taken from Willingale et al. (2013).

<sup>b</sup>The intrinsic absorption, fitted to the spectrum.

<sup>c</sup>The conversion from XRT measured count rate to 0.3–10 keV observed flux.

<sup>d</sup>The conversion from XRT measured count rate to that expected in the *ROSAT* PSPC.

<sup>e</sup>The photon index was unconstrained.

via the service at <http://xmm.esac.esa.int/UpperLimitsServer>.<sup>10</sup> In no cases was the mean XRT brightness above these upper limits at the  $1\sigma$  level, although in one source (discussed below) the flux did

briefly peak above the RASS upper limit. The upper limits for each detected source are given in Table 2.

A second test is to see if the source is variable during the *Swift* observations, particularly whether it is showing significant signs of fading. Such behaviour is expected from explosive transients such as GRBs or SNe; Tidal Disruption Events (TDEs) also fade, although they may undergo a period of  $\sim$  constant flux for some time before fading (Lodato & Rossi 2011). Following Evans et al. (2014) we calculated the Pearson's  $\chi^2$  for each source where we were able

<sup>10</sup> This service also provides upper limits derived from pointed *XMM* observations; however, with the exception of the two sources, which have been previously detected by *XMM*, none of the objects found by XRT have been in the field of pointed *XMM* observations.

**Table 4.** Details of the X-ray sources with catalogue matches.

IceCube field	Source #	SIMBAD match (arcsec)	X-ray match (arcsec)	X-ray flux <sup>a</sup> ( $\times 10^{-13}$ erg cm <sup>-2</sup> s <sup>-1</sup> )
3	1	2MASS J14590700+5931128(2.9 arcsec)	1RXS J145906.5+593105 (8.2 arcsec)	$6.9 \pm 2.4$
5	6	[VV2010c] J083046.9+185707(2.0 arcsec)		
6	6		1WGA J0125.4+1003 (55.6 arcsec)	$4.23 \pm 0.67$
7	1	TYC 76-1038-1(2.9 arcsec)	1RXS J040840.9+033448 (9.7 arcsec)	$11.9 \pm 2.3$
7	3	HD 26292(2.5 arcsec)		
9	2	V* V1296 Tau(3.7 arcsec)	1RXS J040307.5+044427 (22.4 arcsec)	$8.9 \pm 3.2$
9	4	TYC 79-810-1(2.7 arcsec)	1RXS J040428.2+051854 (10.9 arcsec)	$12.5 \pm 3.6$
10	1	[VV2000] J223949.1+060613(6.8 arcsec)	1RXS J223949.7+060610 (13.0 arcsec)	$6.0 \pm 2.5$
11	2	TYC 902-318-1(4.3 arcsec)	1RXS J141546.6+080755 (19.6 arcsec)	$17.9 \pm 4.6$
13	1	MCG+06-24-038(2.0 arcsec)		
13	3	USNO-A2.0 1200-06616808(3.7 arcsec)		
13	4	SDSS J105631.92+354152.8(0.8 arcsec)		
13	5	SDSS J105833.38+361228.3(4.2 arcsec)		
14	1	2MASX J09381483+0200236(1.2 arcsec)	1RXS J093815.6+020026 (10.8 arcsec)	$5.0 \pm 1.6$
14	2	2MASS J09370850+0125440(6.2 arcsec)	1RXS J093708.2+012620 (31.1 arcsec)	$5.5 \pm 2.2$
14	4	SDSS J093909.42+014433.5(5.7 arcsec)		
15	1		1SXPS J185753.6+024012 (5.0 arcsec)	$9.4 \pm 1.6$
15	2	BD+02 3740(4.1 arcsec)	1SXPS J185741.3+024208 (2.6 arcsec)	$2.40 \pm 0.45$
15	3		1SXPS J185809.7+022131 (3.9 arcsec)	$5.4 (+1.4, -1.2)$
16	1	LBQS 1244+1529(2.9 arcsec)		
16	3	2MASS J12453751+1448572(1.5 arcsec)		
16	4	LBQS 1243+1456(1.3 arcsec)		
16	5	[VV2006] J124537.7+145635(4.2 arcsec)		
18	2	1RXS J195826.1+452321(8.7 arcsec)	3XMM J195825.7+452325 (3.3 arcsec)	$1.467 \pm 0.048$
18	3	2MASS J19580115+4518060(6.1 arcsec)	3XMM J195801.1+451805 (6.3 arcsec)	$0.637 \pm 0.017$
19	1	SDSS J102100.35+162554.0(5.0 arcsec)	XMMSL1 J102100.3+162550 (5.5 arcsec)	$37.8 \pm 9.6$
19	2	LP 430-7(3.3 arcsec)		
19	5	SDSS J102118.34+171227.7(3.7 arcsec)		
20	1	HD 162178(8.9 arcsec)		
20	2		XMMSL1 J175016.8+042202 (5.9 arcsec)	$35 \pm 11$

Notes. <sup>a</sup>The catalogued 0.3–10 keV flux. For *ROSAT* objects, this is the catalogued count rate, converted to 0.3–10 keV flux using the conversion from Table 2; for other sources it is the catalogued flux, which is already in the 0.3–10 keV band (1SXPS sources) or the similar 0.2–12 keV band (*XMM* sources).

to produce a light curve (i.e. with more than one bin), using as a model a constant source with count rate set to the mean detected rate for that source. The results of this test are shown in Table 2. The drawback to this method is that it requires binned data, therefore one could argue that the K-S test would be a better indicator of variability. However, many objects show flickering behaviour in X-rays (e.g. Cataclysmic variables), which is not indicative of outbursting. We therefore require not only a measure of variability, but also a light curve that we can inspect, after being prompted by that measure. This implicitly demands binned data, hence our choice of the  $\chi^2$  test.

Only one uncatalogued object (out of 14 for which we can probe variability) has a probability of <10 per cent of being constant, source 4 of field 7; this is the same source which briefly peaked above the RASS upper limit. In the initial observations, the light curve of this source comprised two bins, with evidence for fading at the  $2.3\sigma$  level. We therefore observed the source again repeatedly for a week, but no signs of continued fading were seen (Fig. 3). This source, which is spatially coincident with the USNO-B1 source 0935-0049746, is therefore consistent in behaviour with a background AGN, from which variations of factors of  $\sim 2$  are not uncommon; there is no evidence for a powerful flare that could have produced a high neutrino flux (this would have yielded a much stronger EM flare than that observed). Detailed examination of the IceCube data showed that the event was fully consistent with detection of two neutrinos (i.e. not cosmic ray-induced muons), but the significance

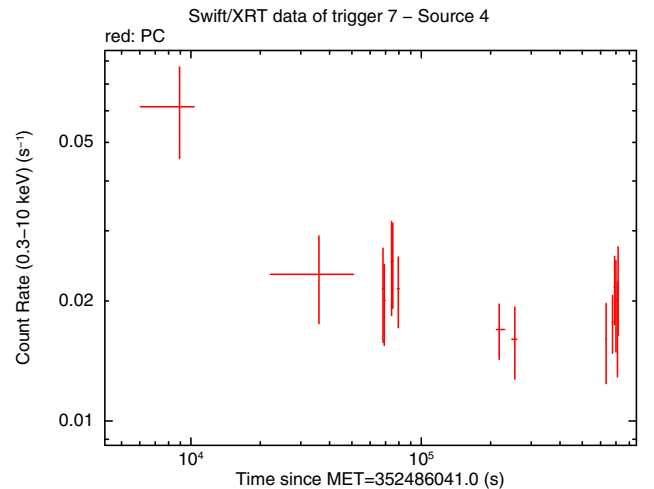


**Figure 3.** Source 4 of the 7th IceCube trigger. This source momentarily peaked above the RASS upper limit for its location, and was fading; however further observations showed the brightness to have levelled off. This is probably a background AGN.

was at the level at which  $\sim 4$  false positives are expected per year. As a final check of this source we re-observed it with *Swift*-XRT on 2014 September 17. In this observation the source was still easily detected, with a count rate of  $\sim 0.03$  ct s<sup>-1</sup>, consistent with the previous



observations and further arguing against its being related to the IceCube trigger.

One other source (source 1 in field 7) also showed strong signs of variability ( $P_{\text{constant}} = 6 \times 10^{-4}$ ), however this was a catalogued X-ray source, 1RXS J040840.9+033448, which SIMBAD<sup>11</sup> lists as a rotationally variable star, and it was a factor of 2 fainter in our observations than in the *ROSAT* catalogue, therefore we do not consider this to be a probable counterpart to the neutrino trigger.

#### 4.2 Probability of serendipity

If we can identify a given source as being unlikely to be serendipitously present in the field of view then it is, conversely, a strong candidate to be the counterpart to the neutrino trigger and worthy of further observation. A simple metric to use to quantify this likelihood is the source brightness. To determine the probability of serendipity for a given source, we first determined the minimum exposure necessary to detect the source: for our detection system we require at least 6 counts, therefore the minimum exposure is  $6/R$  (where  $R$  is the XRT count rate of the source). We then measured the sky area,  $A$ , in our tiled observation which was observed with at least this exposure (accounting for vignetting, overlaps, etc.). We used the  $\log N$ – $\log S$  brightness distribution of extragalactic sources, calculated by Mateos et al. (2008, based on the data in the 2XMM catalogue; Watson et al. 2009) to determine the expected sky density of sources,  $D$ , at least as bright as the detected object in question. The number of expected serendipitous sources in our field of view, at least as bright as the detected object, is  $A \times D$ . This was then multiplied by the completeness of our detection system for the source brightness and exposure time to account for the fact that not all such sources will have been detected. This yields the number of serendipitous sources at least as bright as the detected source that we would expect to detect in our observations. This value is given, for each source, in Table 2.

Only one uncatalogued source (field 18, source 8) was found with a low probability of serendipity. This source is faint, but lies in a region covered by three of the tiled pointings and therefore with a deeper exposure than most of the image. The sky area covered with such an exposure is very low, which is driving the low probability of serendipity. However, the source is flagged as *Poor* by the detection system, meaning that it has a 35 percent probability of being a spurious detection, and the image does not show a strong clustering of events as expected from a point-like source, therefore we think this source is unlikely to be real.

The  $\log N$ – $\log S$  curve of Mateos et al. (2008) was derived only for Galactic latitudes  $|b| > 20^\circ$ , whereas some of the IceCube triggers were at lower Galactic latitudes. We therefore used the 1SXPS catalogue (Evans et al. 2014) to investigate the Galactic dependence of the X-ray source density. For each field in the 1SXPS catalogue, we calculated the density of sources brighter than  $x \text{ ct s}^{-1}$ , for values of  $x = 1 \times 10^{-4}, 3 \times 10^{-4}, 1 \times 10^{-3}, 3 \times 10^{-3}, 1 \times 10^{-2}, 3 \times 10^{-2}, 1 \times 10^{-1}, 3 \times 10^{-1}$ . We did this using the HEALPIX libraries (Górski et al. 2005) with NSIDE = 8192, which results in pixels of area  $0.18 \text{ arcmin}^2$ . Since *Swift* observes many fields multiple times, for each field in 1SXPS we determined for each HEALPIX pixel which observation or stacked image contained the most exposure. Only

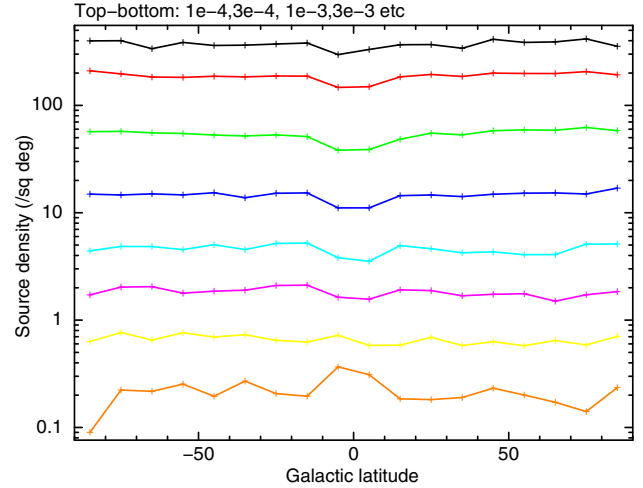


**Figure 4.** The density of X-ray objects above a given flux as a function of Galactic latitude. For bright sources there is a slight increase in the density towards the Galactic Centre, and for fainter sources there is a slight deficit, however the effect is small. For a typical AGN spectrum 1 XRT count corresponds to  $4 \times 10^{-11} \text{ erg cm}^{-2}$ . From top to bottom, the lines correspond to  $10^{-4}, 3 \times 10^{-4}, 10^{-3}, 3 \times 10^{-3}, 10^{-2}, 3 \times 10^{-2}, 10^{-1}, 3 \times 10^{-1} \text{ ct s}^{-1}$ .

that data set and sources detected in it, were considered. For field  $M$ , the density of sources brighter than  $x$  is

$$\Omega_{M,>x} = \sum_N \frac{1}{A_N C_N} \quad (1)$$

where the sum is over all  $N$  sources in the field,  $A_N$  is the area (in the HEALPIX map) covered by the observation in which source  $N$  was detected, and  $C_N$  is the completeness of the 1SXPS catalogue for sources at least as bright as source  $N$  (i.e. for each source we detect, there are  $1/C_N$  actual sources). The overall density as a function of Galactic latitude can then be found simply as

$$\Omega_{b,>s} = \frac{\sum_M \Omega_{M,>s} A_M}{\sum_M A_M}, \quad (2)$$

where the sum is over all fields  $M$  with Galactic latitude  $b$ . We compared our results for  $|b| > 20^\circ$  with Mateos et al. (2008), and found that at XRT count rates below  $\sim 2 \times 10^{-3} \text{ ct s}^{-1}$  (equivalent to  $0.3$ – $10 \text{ keV}$  flux  $\sim 6.3 \times 10^{-14} \text{ erg cm}^{-2} \text{ s}^{-1}$ ) they were in good agreement. At higher count rates we predicted slightly more sources than Mateos et al. (2008), probably because we did not remove from our source list the objects which were the target of the *Swift* observations, whereas Mateos et al. (2008) did, meaning our results are slightly biased. None the less, we can use our results to give an indication of the Galactic latitude dependence of source density, so we split the data into bins of  $5^\circ$  in Galactic latitude; the source density as a function of latitude and count rate is shown in Fig. 4. There is a small effect seen towards the Galactic plane: at most source brightnesses there is a slight reduction in source density at  $|b| < 10^\circ$ , presumably related to the increased absorption in the Galactic plane, however this reduction is less than  $\sim 10$  per cent. At the brightest fluxes there is an increase of  $\sim 40$  per cent in the density of sources at  $|b| < 10^\circ$ , however this is likely to be effected by pointed observations of transient objects, i.e. this does not accurately reflect the density of bright serendipitous sources in the Galactic plane. Based on this analysis, we believe that it is safe to use the extragalactic  $\log N$ – $\log S$  distribution of Mateos et al. (2008) for all of the IceCube triggers, regardless of Galactic latitude.

<sup>11</sup> <http://simbad.u-strasbg.fr/simbad/>

## 5 DISCUSSION AND IMPLICATIONS FOR MULTIMESSENGER ASTRONOMY

We have reported on *Swift*-XRT X-ray follow-up of 20 neutrino triggers from the IceCube observatory. Although we have found 109 X-ray sources, none of them have been identified as a likely counterpart to an IceCube trigger. Conversely, only the 30 objects listed in Table 4 were known prior to the *Swift* observations, and only 16 of them had been detected in X-rays previously; therefore it is very difficult for us to rule out with any degree of confidence that we have detected an EM counterpart to the neutrino trigger, even though we cannot identify it. To investigate further we therefore need to consider what we expect the counterparts to look like in our follow-up observations. Also, IceCube continues to send neutrino triggers to *Swift* and the field of multimessenger astronomy at large is growing rapidly: for example, Advanced LIGO (aLIGO) is expected to be commissioned in early 2015 (Harry et al. 2010). Therefore, it is necessary to consider whether lessons can be learned from the IceCube follow-up presented in this paper, for future EM follow-up on non-EM triggers. Note that we will focus on how to improve our ability to identify the counterpart from among the sources detected in an observation: we do not consider the related issue of how optimally to observe a large (and potentially disjoint) error region; for a discussion of that subject, see Kanner et al. (2012).

Although there are a range of phenomena that can produce neutrino triggers, in this discussion we focus on GRBs (which are also a potential source of gravitational waves), since these have been well studied in the X-ray domain by *Swift* and, as the brightest known transients in the Universe, they represent an upper bound on the detectability of the EM counterparts to neutrino triggers.

### 5.1 How bright will the X-ray counterpart be?

In our analysis (Section 4.1) we looked for, and failed to find, any uncatalogued sources in our data set which were so bright that they would have been catalogued if they were persistent. The lack of such sources may indicate that we did not find the counterpart to the IceCube trigger, or simply that we observed too late after the trigger, when the source had faded below the limit of the existing catalogues. How bright the EM counterpart to a non-EM trigger is at a given time depends on the nature of the emitting object. Here we consider GRBs (Klebesadel, Strong & Olson 1973), since they are expected to be sources of neutrinos and gravitational waves. GRBs are the brightest known EM transients in the Universe, and, although they fade fairly rapidly, they give us a reasonable upper limit on the brightness we may expect from the X-ray counterpart to a non-EM trigger.

The top panel of Fig. 5 shows the distribution of the X-ray flux of GRB afterglows observed with XRT, at a range of times since the trigger. These were derived using the live XRT GRB catalogue<sup>12</sup> (Evans et al. 2009) from which we used the light-curve fits for all GRBs with at least five light-curve bins (i.e. where the fit was reasonably well constrained), and an ECF of  $4.1 \times 10^{11} \text{ erg cm}^{-2} \text{ ct}^{-1}$ , which is the mean value in that catalogue. About 60 per cent of GRBs are expected to be above the typical RASS/XSS sensitivity limit of  $\sim 3 \times 10^{-12} \text{ erg cm}^{-2} \text{ s}^{-1}$  (0.3–10 keV) at one hour after the trigger; this falls to about 15 per cent by eight hours. Comparing this with the delay between the IceCube trigger and the start of the *Swift* observations (Table 1) we would expect that in  $\sim 8$

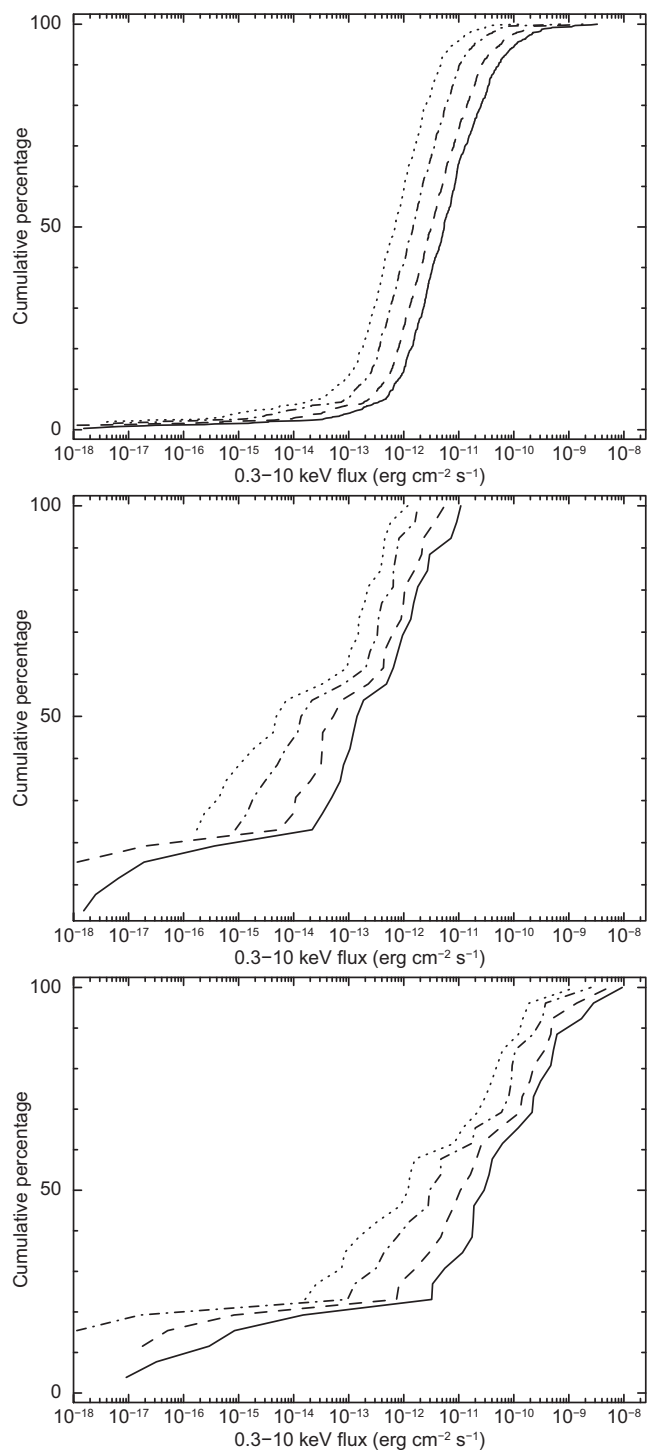


**Figure 5.** The cumulative distribution of the brightness of GRB afterglows detected by the *Swift*-XRT. The solid line showed the flux 1 h after the trigger, the dashed line is 1.8 h after the trigger, and the dot-dashed and dotted lines are for 4 and 8 h after the trigger, respectively. The brightness is taken by evaluating the best-fitting model at these times, which may involve extrapolating past the time a GRB ceases to be detected by *Swift*. The top panel shows all GRBs, the centre panel shows only the short GRBs. The bottom panel is as the centre panel, but with the GRBs shifted to be at a distance of 200 Mpc (assuming the redshifts given in Rowlinson et al. 2013).

<sup>12</sup> [http://www.swift.ac.uk/xrt\\_live\\_cat](http://www.swift.ac.uk/xrt_live_cat)

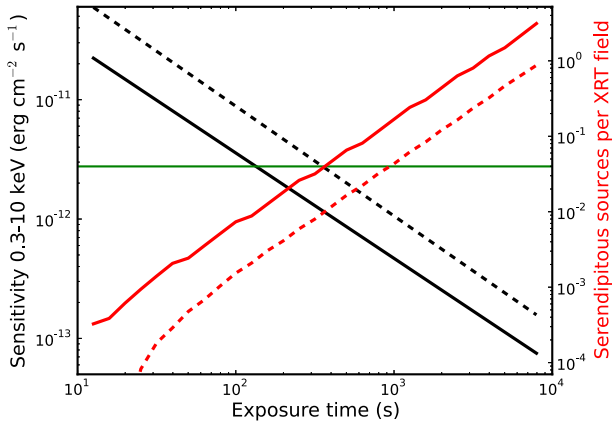


**Figure 6.** The sensitivity of *Swift*-XRT (black lines), and the expected number of serendipitous source expected per XRT field above this limit (red lines), as a function of exposure time. The solid lines correspond to the 50 per cent completeness level, and the dashed lines the 90 per cent completeness level. Note that the two y-axes do not correspond with each other, but are only related via the x-axis and plotted data. The green horizontal line shows the sensitivity limit of the RASS (Voges et al. 1999), corresponding to 0.1 PSPC ct s<sup>−1</sup> (converted to 0.3–10 keV flux assuming the canonical AGN spectrum described in the text), at which level the RASS covers 92 per cent of the sky. The XSS 2–10 keV band limit is at a similar level ( $3 \times 10^{-12}$  erg cm<sup>−2</sup> s<sup>−1</sup>; Warwick et al. 2012).

of cases we should have found an uncatalogued source above the RASS/XSS limit, if the neutrino triggers were related to GRBs. The lack of any such object rules out the idea that all 20 triggers arose from GRBs with  $>99$  per cent (i.e.  $3\sigma$ ) confidence. However, the companion paper to this one (Aartsen et al., in preparation) shows that many (or all) of the neutrino triggers could have been spurious; if even half of the triggers were spurious, this significance drops to below  $3\sigma$ .

The lack of bright sources does not mean that we did not detect a GRB afterglow: in more than half of the triggers, by the time *Swift* observed, the afterglow would have faded below the RASS/XSS limit. However, the ability to identify an afterglow at these lower fluxes is hampered by the density of expected (uncatalogued) sources, as illustrated in Fig. 6. This shows the level (black) at which XRT is 50 and 90 per cent complete (Evans et al. 2014), and the expected number of serendipitous sources (red) per XRT field of view above these levels (Section 4.2) as a function of exposure time. The green line corresponds to the typical RASS/XSS limit. The XRT 90 per cent completeness level reaches the RASS and XSS limits in an exposure of  $\sim 350$  s; and we expect  $\sim 0.01$  serendipitous sources per XRT field with fluxes above this limit. That is, in a 7-tile observation such as those reported in this paper, any detected source below the flux limit set by the existing large-area catalogues, will have a probability of being serendipitous of  $\geq 0.07$ , i.e. we cannot expect to identify the counterpart with even  $2\sigma$  confidence.

It is impossible therefore, for us to identify the counterpart to the neutrino triggers reported in this paper based on the source flux at detection, and in any future follow-up of astrophysical neutrinos, we would expect at best 50 per cent of GRB afterglows to be identified in this way.

While neutrinos are expected from all GRBs, a prime candidate for the sources of gravitational waves are nearby short GRBs, which arise from the merging of two neutron stars. The middle panel of Fig. 5 shows the flux distribution of the short GRBs detected

by the *Swift*-XRT: they are much fainter than long GRBs and we are unlikely to observe any before they fall below the limits of existing catalogues. However, the horizon distance of aLIGO is around 200 Mpc (Abadie et al. 2010a), whereas the average short GRB redshift in the *Swift* sample is 0.72 (Rowlinson et al. 2013), corresponding to a luminosity distance of  $\sim 4000$  Mpc. Thus on-axis short GRBs detected by aLIGO should be a factor of  $\sim 400$  brighter than those detected by *Swift*, although the time axis of the light curve is compressed by the reduced time dilation, which shortens any plateau phase. In the bottom panel of Fig. 5, we have shifted the XRT afterglows from the redshifts given in Rowlinson et al. (2013) to 200 Mpc ( $z = 0.045$ ). In this case  $\sim 80$  per cent of short GRBs would be above the RASS limit one hour after the trigger, and 50 per cent would still be that bright at eight hours. These results are less optimistic than those reported by Kanner et al. (2012), however they used only short GRBs with known redshift (giving a smaller sample), whereas we have included short GRBs with no known redshift, assigning to them the mean short GRB redshift of 0.72. It should also be noted, that in ten years of operation, *Swift* has not yet detected a short GRB less than 500 Mpc away (GRB 061201,  $z = 0.111$ ; Berger 2006), and indeed no short GRB thousands of times brighter than the typical *Swift* short GRBs has been reported in over twenty years of observations by various facilities. This tells us that nearby short GRBs, which may trigger aLIGO, are extremely rare.

### 5.1.1 Increasing the sensitivity

Our ability to identify a counterpart by its brightness would be enhanced if we had a more sensitive reference catalogue. For example, Fig. 6 shows that if *Swift*-XRT had conducted a 2 ks observation of a field prior to an IceCube trigger, then the list of known sources at that location would be 90 per cent complete down to a flux five times below the RASS limit; for hard or absorbed sources the increase in sensitivity is significantly more pronounced. At such levels, 95 per cent (50 per cent) of the *Swift*-detected GRBs would be bright enough to be confirmed as new (non-serendipitous) sources in an observation at one (eight) hours after the trigger.

To pre-image the entire sky with *Swift*-XRT, at 2 ks per field, is clearly not practical (it would require around 18 yr of observing time!), although some subset of the sky, for example, corresponding to the galaxies deemed most likely to yield a short GRB that aLIGO would detect, could potentially be observed. The forthcoming *eRosita* mission, expected to launch in 2016, will produce an all-sky survey in the 0.2–10 keV band which will be a factor of 30 more sensitive than the RASS (Cappelluti et al. 2011). This will provide a valuable resource for identifying new sources in *Swift*-XRT observations of non-EM triggers. In the meantime, catalogues such as the 1CSC (Evans et al. 2010), 3XMMi-DR4 (Watson et al., in preparation) and 1SXPS (Evans et al. 2014) could be used when available, but their sky coverage is very limited.

## 5.2 Identifying counterparts by fading light curves

Transient events by definition fade over time. However, in our follow-up observations, only 19 (out of 109) sources were bright enough (or observed for long enough) to yield two or more light curve bins, and 12 of these occurred in the field of trigger #7, which was observed for an unusually long time to allow us to rule out the possible counterpart in that field (Section 4.1). Also, not all transient sources fade on the time-scale of a single observation. GRBs,

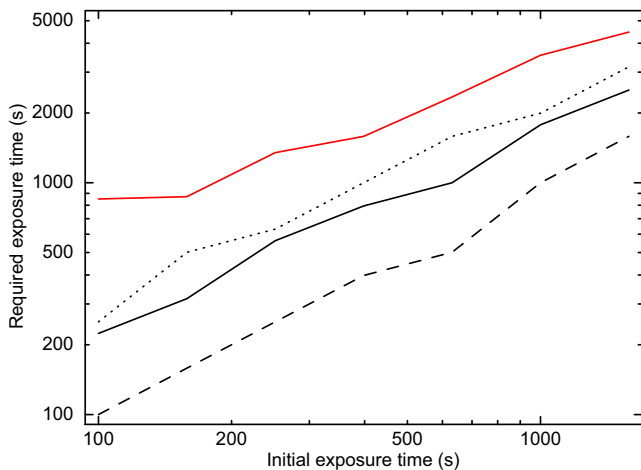


**Figure 7.** The minimum second-observation exposure time needed to detect the fading of a source as a function of the exposure time in the initial image. The source brightness in the first observation is that at which our detection system is 50 per cent complete in the initial exposure time. If the source is detectable in the second observation, the black (red) solid line shows the minimum time needed to detect the source in the second image, and measure the count rate as  $2\sigma$  ( $3\sigma$ ) fainter than in the initial image. If the source is not detectable in the second image, the black dotted line shows the exposure time needed to obtain a  $3\sigma$  upper limit inconsistent with the initial brightness if the source is only just below the detection threshold; the black dashed line is that needed if the source has faded away completely. See Section 5.2 for full details.

for example, tend to fade quickly, but many show a ‘plateau’ phase where there is little or no decay (Nousek et al. 2006; Zhang et al. 2006); TDEs similarly begin with a period of roughly constant flux before beginning their decay (Lodato & Rossi 2011). To discover whether a source is fading it is therefore necessary to perform repeat observations, and if the type of transient is not known, then several such observations are needed, with increasing delays since the trigger to account for different progenitor types. While this strategy was not employed for the neutrino triggers reported in this paper, such an approach should be considered in the future, given the lack of identified counterparts in this work.

In order to confirm fading, these extra observations need to be of sufficient exposure for us to either measure the count rate accurately enough to confirm a decay with some predetermined level of significance, or find an upper limit below the level of the previous detection. To accurately determine how much exposure is needed requires knowledge of the source light curve. As a generic approach, we can determine the count rate  $R_2$  in the second observation which allows us to confirm fading in the shortest possible exposure time.<sup>13</sup> Since the optimal value of  $R_2$  is not a priori obvious, we stepped it over the range  $0.001R_1 - 0.99R_1$ , finding the value which gave the minimum exposure time needed to detect fading at the  $2\sigma$  and  $3\sigma$  levels. These are shown in Fig. 7, where we plot the initial exposure ( $E_1$ ) on the x-axis, and take  $R_1$  as the count rate at which the source detection algorithm is 50 per cent complete in that exposure time. If  $R_2$  was below the detection threshold in the second observation, we

found the exposure time that would be needed to give a  $3\sigma$  upper limit on the count rate that was below the  $1\sigma$  lower bound on  $R_1$ . We did this for two cases: where the  $R_2$  was just below the detection threshold (i.e. the source contributed five counts to XRT data set), and where the source had completely vanished (it contributed no photons); these are plotted as the dotted lines in Fig. 7.

From this we see that a typical repeat observation will need to be at least a factor of 2 longer than the initial exposure; unless prior knowledge of the source type means that we expect the source to have faded away completely by the time of the second observation. However, this does not mean that the total observing time needs to be doubled. The goal of the follow-up observations is to determine whether any of the uncatalogued sources detected in the first observation have faded, not to search for new sources. Therefore, only those fields containing uncatalogued sources need to be re-observed. We suggest that a modest investment of observing time spent on observations of the newly-discovered X-ray sources would significantly increase the likelihood of identifying an X-ray counterpart to a non-EM trigger using *Swift* – provided that the source was detected in the initial observation.

We can determine with more confidence the exposure time needed to determine fading if we know in advance what the source light curve looks like. One of the main candidates to provide a gravitational wave + EM detection are short GRBs, and thanks to *Swift* we have some idea of their X-ray light-curve morphology. We took from the short GRBs listed in Rowlinson et al. (2013) those which triggered *Swift* and for which the live XRT GRB catalogue contains light-curve fits (i.e. at least two light-curve bins, excluding upper limits). Then, assuming an initial exposure of 500 and 1000 s, starting 1, 2 and, 4 h after the GRB trigger, we determined how many of those GRBs would be detected by *Swift*, and at what brightness. We then determined how long a second observation would have to be in order to confirm that the source had faded at the  $3\sigma$  level, as a function of the delay between the first and second observations. We considered a source to have faded either if it was detectable, and had a measured count rate inconsistent with the initial rate at the  $3\sigma$  level, or if it was undetected with a  $3\sigma$  upper limit inconsistent with that rate. The results are shown in the top panels of Fig. 8, in which we show the exposure time needed to detect fading in 50 and 90 per cent of the bursts as a function of the time between observations. Note that ‘50 per cent of the bursts’ means 50 per cent of the short GRBs that would have been detected in the initial observation. The shorter that observation is, or the longer after the trigger it begins, the fewer the bursts detected in the initial observation. Therefore (for example) the black curve in the top-left panel of Fig. 8 was compiled from 11 GRBs, whereas the red curve in the same panel was compiled from 9 GRBs; the sample from Rowlinson et al. (2013) contains 43 bursts.<sup>14</sup> This explains why the necessary exposure is surprisingly short at some times: only the brightest bursts are detectable, but for these bright bursts, it is relatively simple to identify fading. For some GRBs, we were not able to confirm fading with  $3\sigma$  confidence if the delay between observations was too short, with the second observation’s exposure extending to a maximum of  $10^5$  s; for the purposes of plotting, we set the necessary exposure time in these objects to be  $10^6$  s (i.e. off the scale). For shorter delay times it is sometimes not possible to determine fading in even 50 per cent of cases; the only solution is

<sup>13</sup> This is a function of the background level and the size of region over which source counts are accumulated. We set the background to  $10^{-6}$  ct  $s^{-1}$  pixel $^{-1}$ , the mean value from the ISXPS catalogue (Evans et al. 2014), and set the region size to be that used by the XRT auto-analysis software for the brightness of the source in the initial observation; see table 1 of Evans et al. (2007).

<sup>14</sup> Since we can’t measure fading in objects we don’t detect, and we are interested in how to detect fading, not how to detect the GRB in the first place, this approach is the most informative.



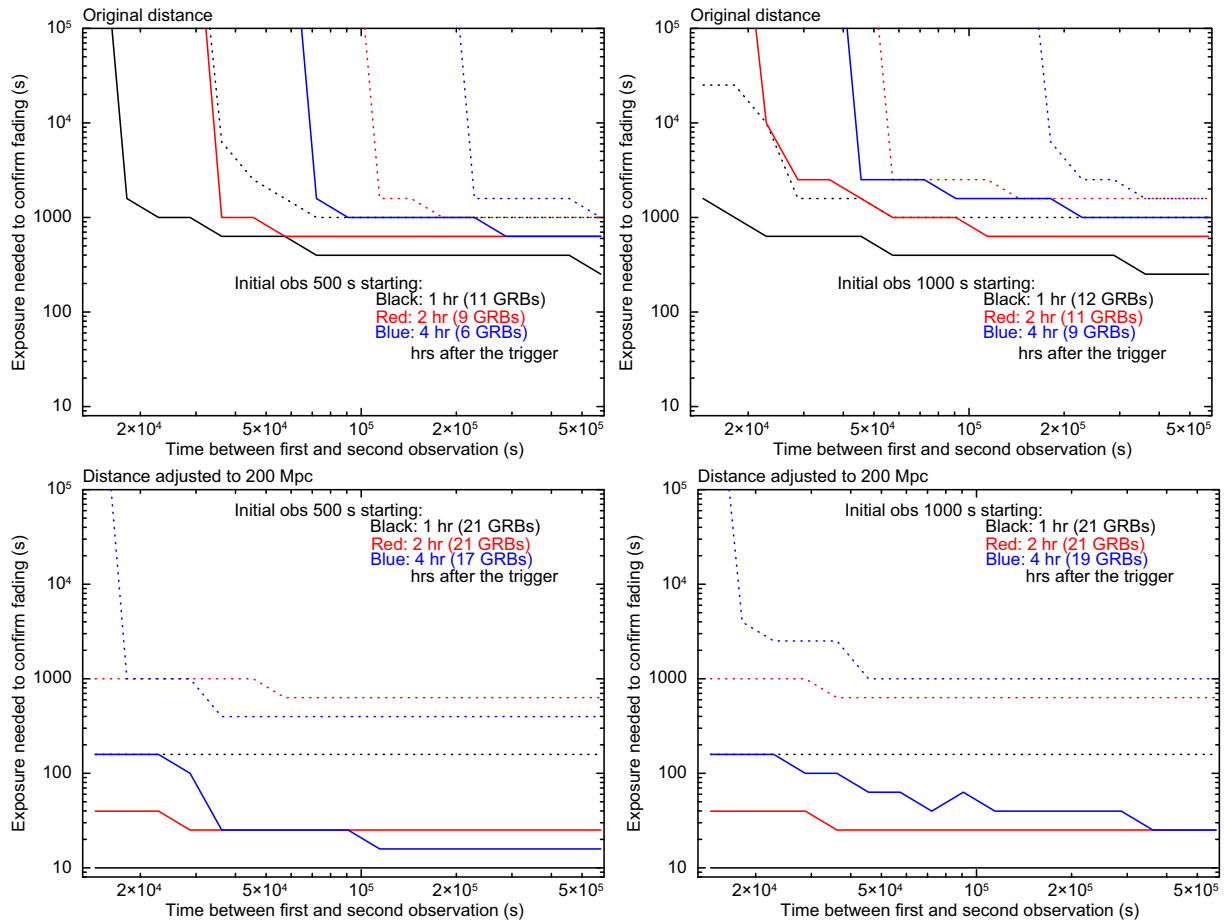


**Figure 8.** The exposure time necessary in a follow-up observation of a short GRB needed to confirm fading at the  $3\sigma$  level, as a function of the delay between the initial and follow-up observations. The solid (dotted) lines are the exposure needed for 50 percent (90 percent) of the short GRBs detected in the initial observation to be confirmed fading at the  $3\sigma$  level. The black, red, and blue lines are for an initial observation beginning 1, 2 and 4 h after the GRB trigger, respectively. The numbers in the legend indicate the number of GRBs corresponding to 100 percent for each data set, i.e. the number of GRBs that would have been detected in the initial observation. This is from a total of 43 GRBs which are input to the simulations. Left: for an initial observation of 500 s. Right: for an initial observation of 1000 s. In the bottom panels we have adjusted the light curves of the short GRBs as if the GRB was at 200 Mpc, using the redshifts and GRB list given in Rowlinson et al. (2013). In the top panels, the GRB light curves as detected by *Swift* were used. The point where the lines stop decaying reflects corresponds to the point at which the 50th or 90th percentile becomes too faint to detect, i.e. to confirm fading we require an upper limit below the level of the initial detection. This level, and hence the time needed to generate the upper limit, does not depend on the time between observations.

to wait longer before performing the second observation. Note also that for simplicity we assumed that the second observation was a continuous one, i.e. we ignored the fact that *Swift* can observe a given target for a maximum of 2.7 ks every  $\sim 5.7$  ks orbit.

As noted earlier (Section 5.1), the mean redshift of *Swift* short GRBs is  $\sim 0.7$ , whereas for aLIGO the maximum distance to a short GRB is expected to be 200 Mpc ( $z \sim 0.045$ ). Therefore we repeated the above calculations, first shifting the GRB to be at 200 Mpc. We used the redshifts from Rowlinson et al. (2013), i.e. reverting to the mean ( $z = 0.72$ ) where it is not known. The results of this are shown in the bottom panels of Fig. 8. Not surprisingly, fading is much easier to detect when the GRB is nearby; indeed, if we can detect a GRB at 200 Mpc within 4 h of the trigger, then we should be able to confirm fading at most 8 h later.

## 6 CONCLUSIONS

We have used the *Swift*-XRT to observe 20 IceCube neutrino-doublet triggers, covering the IceCube error circle in seven tiled

observations. We find 109 X-ray sources, only 16 of which had been detected in X-rays before these observations were taken. However, none of the uncatalogued sources are bright enough to be distinguished from the serendipitous sources expected in a 7-tile XRT observation. Given the behaviour of GRB afterglows observed by the *Swift*-XRT, this lack of bright counterparts allows us to rule out with  $>99$  percent confidence that the neutrino triggers arise exclusively from GRBs. In only one case could we identify signs of fading in these single observations, and follow-up observations showed that this was not a transient object.

Considering the wider question of using *Swift*-XRT to detect the counterpart to non-EM triggers, such as PeV neutrinos or gravitational wave triggers from the Advanced-LIGO facility, we have shown that a deeper all-sky X-ray catalogue than the RASS, such as that which will be created by *eRosita*, will make it easier to identify a counterpart simply from its flux in the initial observation. However, a better and more immediately available approach will be to probe source variability, in particular, searching for fading. Re-observing every uncatalogued X-ray source detected by XRT



in the initial follow-up observations, with at least twice the initial exposure time, should enable us to identify any source which has faded at the  $3\sigma$  level.

For a short GRB at a distance of 200 Mpc – as aLIGO expects to discover – with its jet pointed towards Earth, an initial observation within a few hours of the trigger, followed by a second observation of 2 ks, 8 h after the first, should be sufficient to confirm fading in almost all cases (if the GRB was detected in the initial observation), provided the afterglows of such GRBs are of the same luminosity and morphology distributions as the sample of short GRBs detected to date by *Swift*.

While we have demonstrated techniques to maximize the potential for multimessenger astronomy with *Swift*, a sensitive, all-sky (or at least large field-of-view) X-ray imager, ideally with some form of gamma-ray detector to rapidly distinguish GRBs from other X-ray transients, would be the ideal facility with which to locate the high-energy counterparts to non-EM-detected transients.

## ACKNOWLEDGEMENTS

This work made use of data supplied by the UK Swift Science Data Centre at the University of Leicester. PAE and JPO acknowledge UK Space Agency support. JMG gratefully acknowledges the support from NASA under award NNN13CH61C. We thank the anonymous referee for their helpful and constructive feedback on the manuscript.

## REFERENCES

- Aartsen M. G. et al., 2013, *Phys. Rev. Lett.*, 111, 021103  
 Abadie J. et al., 2010a, *Class. Quantum Gravity*, 27, 173001  
 Abadie J. et al., 2010b, *ApJ*, 715, 1453  
 Abbasi R. et al., 2011, *Phys. Rev. Lett.*, 106, 141101  
 Abbasi R. et al., 2012, *Nature*, 484, 351  
 Abbasi R. et al., 2014, *A&A*, 563, C1  
 Abbott B. P. et al., 2009, *Rep. Prog. Phys.*, 72, 076901  
 Abraham J. et al., 2010, *Phys. Lett. B*, 685, 239  
 Accadia T. et al., 2012, *J. Instrum.*, 7, 3012  
 Achterberg A. et al., 2006, *Astropart. Phys.*, 26, 155  
 Adrián-Martínez S. et al., 2013, *A&A*, 559, A9  
 Alekseev E. N., Alekseeva L. N., Volchenko V. I., Krivosheina I. V., 1987, *J. Exp. Theor. Phys. Lett.*, 45, 589  
 Arnaud K. A., 1996, in Jacoby G. H., Barnes J., eds, *ASP Conf. Ser. Vol. 101, Astronomical Data Analysis Software and Systems V*. Astron. Soc. Pac., San Francisco, p. 17  
 Asano K., Mészáros P., 2014, *ApJ*, 785, 54  
 Berger E., 2006, *GCN Circ.*, 5952, 1  
 Bionta R. M., Blewitt G., Bratton C. B., Casper D., Ciocio A., 1987, *Phys. Rev. Lett.*, 58, 1494  
 Burrows D. N. et al., 2005, *Space Sci. Rev.*, 120, 165  
 Butler N. R., 2007, *AJ*, 133, 1027  
 Cappelluti N. et al., 2011, *Mem. Soc. Astron. Ital. Suppl.*, 17, 159  
 Evans P. A. et al., 2007, *A&A*, 469, 379  
 Evans P. A. et al., 2009, *MNRAS*, 397, 1177  
 Evans I. N. et al., 2010, *ApJS*, 189, 37  
 Evans P. A. et al., 2012, *ApJS*, 203, 28  
 Evans P. A. et al., 2014, *ApJS*, 210, 8  
 Gehrels N. et al., 2004, *ApJ*, 611, 1005  
 Goad M. R. et al., 2007, *A&A*, 476, 1401  
 Górski K. M., Hivon E., Banday A. J., Wandelt B. D., Hansen F. K., Reinecke M., Bartelmann M., 2005, *ApJ*, 622, 759  
 Harry G. M. et al., 2010, *Class. Quantum Gravity*, 27, 084006  
 Hinton J. A. et al., 2004, *New Astron. Rev.*, 48, 331  
 Hirata K., Kajita T., Koshihara M., Nakahata M., Oyama Y., 1987, *Phys. Rev. Lett.*, 58, 1490  
 Hirata K. S. et al., 1988, *Phys. Rev. D*, 38, 448  
 Kachelrieß M., Tomàs R., Buras R., Janka H.-T., Marek A., Rampp M., 2005, *Phys. Rev. D*, 71, 063003  
 Kanner J., Camp J., Racusin J., Gehrels N., White D., 2012, *ApJ*, 759, 22  
 Klebesadel R. W., Strong I. B., Olson R. A., 1973, *ApJ*, 182, L85+  
 Kraft R. P., Burrows D. N., Nousek J. A., 1991, *ApJ*, 374, 344  
 Kunkel W. et al., 1987, *IAU Circ.*, 4316, 1  
 Lodato G., Rossi E. M., 2011, *MNRAS*, 410, 359  
 Mateos S. et al., 2008, *A&A*, 492, 51  
 Moretti A. et al., 2007, in O'Dell S. L., Pareschi G., eds, *Proc. SPIE Conf. Ser. Vol. 6688, Optics for EUV, X-Ray, and Gamma-Ray Astronomy III*. SPIE, Bellingham, p. 66880G  
 Nousek J. A. et al., 2006, *ApJ*, 642, 389  
 Pfeiffermann E. et al., 1987, in Koch E., Schmahl G. A., eds, *Proc. SPIE Conf. Ser. Vol. 733, Soft X-ray Optics and Technology*. SPIE, Bellingham, p. 519  
 Rowlinson A., O'Brien P. T., Metzger B. D., Tanvir N. R., Levan A. J., 2013, *MNRAS*, 430, 1061  
 Saxton R. D., Read A. M., Esquej P., Freyberg M. J., Altieri B., Bermejo D., 2008, *A&A*, 480, 611  
 Skrutskie M. F. et al., 2006, *AJ*, 131, 1163  
 Voges W. et al., 1999, *A&A*, 349, 389  
 Warwick R. S., Saxton R. D., Read A. M., 2012, *A&A*, 548, A99  
 Watson M. G. et al., 2009, *A&A*, 493, 339  
 Willingale R., Starling R. L. C., Beardmore A. P., Tanvir N. R., O'Brien P. T., 2013, *MNRAS*, 431, 394  
 Zhang B., Fan Y. Z., Dyks J., Kobayashi S., Mészáros P., Burrows D. N., Nousek J. A., Gehrels N., 2006, *ApJ*, 642, 354

This paper has been typeset from a  $\text{\LaTeX}$  file prepared by the author.